Journal of Computational Physics **159,** 344–376 (2000)
doi:10.1006/jcph.2000.6450, available online at http://www.idealibrary.com on IDEAL®

An ELLAM-MFEM Solution Technique for Compressible Fluid Flows in Porous Media with Point Sources and Sinks

Hong Wang,* Dong Liang,*,†,[1] Richard E. Ewing, ‡,[2] Stephen L. Lyons,§ and Guan Qin

*Department of Mathematics, University of South Carolina, Columbia, South Carolina 29208; †School of Mathematics and System Sciences, Shandong University, Jinan, Shandong 250100, China; ‡Institute for Scientific Computation, Texas A&M University, College Station, Texas 77843-3404; §Upstream Strategic Research Center, Mobil Technology Company, 13777 Midway Road, Dallas, Texas 75244-4390

Received April 19, 1999; revised January 14, 2000

We develop an ELLAM-MFEM solution procedure for the numerical simulation of compressible fluid flows in porous media with point sources and sinks. An Eulerian–Lagrangian localized adjoint method (ELLAM), which was previously shown to outperform many widely used and well-regarded methods in the context of linear transport partial differential equations, is presented to solve the transport equation for concentration. Since accurate fluid velocities are crucial in numerical simulations, a mixed finite element method (MFEM) is used to simultaneously solve the pressure equation as a system of first-order partial differential equations for the pressure and mass flow rate. This minimizes the numerical difficulties occurring in standard methods caused by differentiation of the pressure and then multiplication by rough coefficients.

Computational experiments show that the ELLAM-MFEM solution procedure can accurately simulate compressible fluid flows in porous media with coarse spatial grids and very large time steps, which are one or two orders of magnitude larger than those used in many numerical methods. The ELLAM-MFEM solution technique symmetrizes the governing partial differential equations, and greatly reduces or eliminates non-physical oscillation and/or excessive numerical dispersion present

[1] This author acknowledges support from the University of South Carolina.

[2] This author acknowledges support from NSF Grants DMS-9626179, DMS-9706985, DMS-9707930, NCR9710337, DMS-9972147, and INT-9901498; EPA Grant 825207; two generous awards from Mobil Research and Development; and Texas Higher Education Coordinating Board Advanced Research and Technology Program Grants 010366-168 and 010366-0336.

0021-9991/00 $35.00

in many large-scale simulators that are widely used in industrial applications. It conserves mass and treats boundary conditions in a natural manner. It can treat large adverse mobility ratios, discontinuous permeabilities and porosities, anisotropic dispersion in tensor form, compressible fluid, heterogeneous media, and point sources and sinks.

Key Words: advection–diffusion equations; characteristic methods; compressible flows; Eulerian–Lagrangian methods; point sources and sinks; porous medium flows.

CONTENTS

1. INTRODUCTION

The objective of petroleum reservoir simulation, environmental modeling, and many other important applications is to predict the complex chemical, physical, and fluid flow processes occurring in subsurface porous media sufficiently well to optimize the recovery of hydrocarbon or to accurately predict and thoroughly remediate the contamination in groundwater, etc. In order to do this, one must build mathematical models to describe the essential phenomena and the fundamental laws, and design numerical methods to discretize these models and to represent the basic features as well as possible without introducing serious nonphysical phenomena. The mathematical models used to describe these complex fluid flow processes are strongly coupled nonlinear systems of partial differential equations (PDEs) and constraining equations. These systems are characterized by strong nonlinearity and coupling among these equations, the advection dominance of the transport equation and the moving steep fronts present in the solutions to this equation, the singularities of the solutions at point sources and sinks (i.e., injection and production wells), the compressibility of the fluid mixture and the medium, the strong heterogeneity of the media, the large adverse mobility ratio in the fluid flow processes, the anisotropic dispersion in tensor form, the enormous size of field-scale application, and the required long time period of prediction. Because of these salient features, the numerical simulation to these systems encounters severe difficulties.

Space-centered finite difference or finite element methods (FDMs, FEMs) often generate numerical solutions with severe non-physical oscillations. In industrial applications, upstream weighting techniques are commonly used to stabilize the numerical approximations to these systems in large-scale simulators. However, these methods produce excessive artificial numerical dispersion and potentially spurious effects related to the orientation of the grid [24]. Many attempts have been made to develop numerical methods that overcome these difficulties and allow accurate numerical solutions with reasonable computational effort. High-resolution methods, such as the Godunov methods, the total variation diminishing methods (TVD), and the essentially non-oscillatory (ENO) methods, are well suited for the

solution of nonlinear hyperbolic conservation laws and the resolution of shock discontinuities in the solutions without excessive smearing or spurious oscillations [16, 18, 23, 31, 50, 51, 53]. Moreover, they conserve mass. High-resolution methods have been successfully applied in aerodynamics, where the fluids are highly compressible and flows exhibit shock discontinuities, and have generated very satisfactory results. But these methods are mostly explicited; the size of the time steps in these methods is subject to the CFL constraint. Few references could be found in the literature on the application of high-resolution methods to porous medium flows, especially in the presence of strongly heterogeneous and compressible media as well as point sources and sinks.

Because of the hyperbolic nature of advective transport, characteristic methods have been investigated extensively in numerical simulations of porous medium flows [8, 17, 22, 29, 37, 39–41, 54]. Characteristic methods follow the movement of information or particles as well as their interactions. Because the solutions are much smoother along the characteristics than they are in the time direction, characteristic methods allow large time steps to be used in numerical simulations while still maintaining their stability and accuracy. But characteristic methods usually require extra implementational effort and raise many implementational and analytical issues that need to be addressed. Traditional forward or particle tracking methods advance the grids following the characteristics. They greatly reduce temporal errors and, thus, generate fairly accurate solutions even if large time steps are used. However, they often distort the evolving grids severely and greatly complicate the solution procedure. The modified method of characteristics (MMOC) follows the flow direction by tracking the characteristics backward from a fixed grid at the current time step and hence avoids the grid distortion problems present in forward tracking methods [22]. The MMOC symmetrizes and stabilizes the governing PDEs, greatly reducing temporal errors and therefore allowing for large time steps in a simulation without the loss of accuracy and eliminating the excessive numerical dispersion and grid orientation effects present in many Eulerian methods [24, 47]. However, many previous characteristic methods fail to conserve mass and have difficulties in treating boundary conditions.

Douglas *et al*. presented and analyzed a sequential linearization solution procedure for the miscible displacement of one incompressible fluid by another in a porous medium, in which mixed finite element methods (MFEMs) are employed to approximate the pressure, and the Darcy velocity and Galerkin FEMs are used to approximate the concentration [20, 21]. Russell first introduced the MMOC into the SPE literature in solving the transport equation in the system of incompressible fluid flow for reservoir simulation, where the pressure equation was solved by an FEM with piecewise biquadratic trial and test functions [45]. Ewing, Russell, and Wheeler combined the ideas [20, 21, 45] and proposed an improved MMOC-MFEM sequential solution procedure [27] for the miscible displacement of incompressible fluid flow by using the MMOC to approximate the transport equation and an MFEM for the pressure equation. The use of MFEM yields accurate Darcy velocity fields, to conserve mass that conserves mass, while the application of MMOC allows large time steps to be used in solving the transport equation without loss of accuracy and eliminates the numerical dispersion and grid orientation effects, which are among the major difficulties presented in large-scale reservoir simulators widely used in industry applications [4, 6, 15, 24, 28, 38]. However, the MMOC-MFEM solution procedure fails to conserve mass and treats boundary conditions in an *ad hoc* manner, which seriously affects its application. Finally, despite the large amount of research conducted on the numerical simulation of incompressible fluid flows, few numerical experiments have been reported in the literature on numerical

simulations to compressible fluid flows in porous media, especially with characteristic methods.

The Eulerian–Lagrangian localized adjoint method (ELLAM) was first presented by Celia, Russell, Herrera, and Ewing in solving one-dimensional (constant-coefficient) advection–diffusion PDEs [13, 33]. The ELLAM methodology provides a general characteristic solution procedure for advection–diffusion PDEs and a consistent framework for treating general boundary conditions and maintaining mass conservation. Thus, it overcomes the two principal shortcomings of previous characteristic methods while maintaining their numerical advantages. For example, like the MMOC schemes [22, 27] and many other characteristic methods, the ELLAM schemes can solve advection–diffusion PDEs accurately regardless of whether the advection or diffusion term dominates the flow process. In fact, when diffusion dominates a fluid process, the governing transport PDE behaves like a parabolic PDE. Virtually all numerical methods work well in this case. The authors previously carried out numerical experiments in the context of one- and two-dimensional linear transport PDEs [1, 55–57]. These results show that the ELLAM schemes often outperform many widely used and well-regarded methods.

In this paper we develop an ELLAM-MFEM solution procedure for compressible fluid flows in porous media with point sources and sinks, which have much stronger coupling and nonlinearity than incompressible fluid flows. In the ELLAM-MFEM solution procedure, we use an ELLAM scheme for the transport equation and an MFEM method for the pressure equation, and derive an iterative procedure for the system of compressible fluid flow. The ELLAM-MFEM solution procedure can simulate compressible fluid flow in porous media accurately with coarse spatial grids and very large time steps, which are much larger than the time steps used in the MMOC-MFEM sequential solution procedure and one or two orders of magnitude larger than those used in many large-scale simulators. In this manner, the ELLAM-MFEM solution technique has a greatly improved computational efficiency over many other methods. The ELLAM-MFEM technique can treat large adverse mobility ratios, discontinuous permeabilities and porosities, anisotropic dispersion in tensor form, compressible fluid, heterogeneous media, and point sources and sinks.

The rest of this paper is organized as follows. In Section 2, we derive a mathematical model for compressible fluid flows in porous media. In Section 3, we outline an MFEM scheme for the parabolic pressure equation. In Section 4, we present an ELLAM scheme for the transport equation. In Section 5, we derive an ELLAM-MFEM solution procedure for the system of compressible flow. In Section 6, we perform different types of numerical experiments to demonstrate the strength of the ELLAM-MFEM solution procedure. In Section 7, we summarize the results and draw conclusions.

2. A MATHEMATICAL MODEL FOR COMPRESSIBLE FLUID FLOWS IN POROUS MEDIA

In this section, we derive a mathematical model for describing compressible fluid flow processes in porous media that arise in petroleum reservoir simulation, subsurface contaminant transport and remediation, and other applications. In these problems, the fluid flow processes are governed by the mass conservation for the total fluid mixture and for the invading fluid or solvent, Darcy's law for momentum, and equations of state that provide fluid properties.

2.1. Conservation of Mass for the Fluid Mixture

In this subsection, we derive a governing differential equation that describes the conservation of mass for the total fluid mixture. We consider a fluid flow process, in which the invading fluid and the resident fluid are fully miscible and flow together as one phase fluid in the porous medium. Because in many cases the thickness of the physical domain is significantly smaller than its horizontal length and width, we assume that the fluid flow process is vertically homogeneous by averaging the physical quantities and medium properties in the vertical direction and we assume the physical domain $\Omega \subset \mathbb{R}^2$ with a nonuniform local elevation. Let $\mathbf{u}(\mathbf{x}, t) = (u_x(\mathbf{x}, t), u_y(\mathbf{x}, t))$ be the Darcy (superficial) velocity of the fluid mixture, let ρ be the mass density of the fluid mixture, and let ϕ be the porosity of the medium (fraction of the total volume available for fluid flow). Let $A \subset \Omega$ be any representative volume element; then the conservation of mass states that the rate of mass accumulated within A equals the rate of mass flowing into A across the boundary ∂A of A plus the net amount of mass injected into A via sources and sinks. This statement can be expressed in an integral form mathematically,

$$\frac{d}{dt}\int_A \phi\rho \, d\mathbf{x} = -\int_{\partial A} \rho\mathbf{u}\cdot\mathbf{n}\, dS + \int_A q \, d\mathbf{x}, \tag{2.1}$$

where $\mathbf{n} = (n_x, n_y)$ is the unit outward normal to the boundary ∂A, and q is the source and sink term that represents the mass flow rate per unit volume injected into (or produced from) the volume element A.

Applying the divergence theorem, we get

$$\int_A \frac{\partial}{\partial t}(\phi\rho)\, dx = \int_A (-\nabla\cdot(\rho\mathbf{u}) + q)\, d\mathbf{x}. \tag{2.2}$$

This is in turn written as the following partial differential equation since Eq. (2.2) holds for arbitrary $A \subset \Omega$:

$$\frac{\partial}{\partial t}(\phi\rho) = -\nabla\cdot(\rho\mathbf{u}) + q, \qquad \mathbf{x}\in\Omega, \quad t\in(0,T]. \tag{2.3}$$

2.2. Conservation of Mass for the Solute/Solvent in the Fluid Mixture

Let c be the concentration (mass fraction) of the injected fluid of the concerned solute/solvent in the fluid mixture. We can derive a governing differential equation that describes the conservation of mass for the concerned component as Eq. (2.1). But in this case, we also need to take into account the effect of the physical diffusion and dispersion of the component in the fluid mixture. Hence, the conservation of mass is expressed as

$$\frac{d}{dt}\int_A \phi\rho c \, d\mathbf{x} = -\int_{\partial A} \rho(\mathbf{u}c - \mathbf{D}(\mathbf{u})\nabla c)\cdot\mathbf{n}\, dS + \int_A qc^* \, d\mathbf{x}, \tag{2.4}$$

where $(\mathbf{u}c - \mathbf{D}(\mathbf{u})\nabla c)$ is the total (volumetric) flux flowing into A across the boundary ∂A of A. c^* is a prescribed concentration at sources (or injection wells) or is equal to c at sinks. The physical diffusion–dispersion tensor consists of molecular diffusion and (anisotropic velocity-dependent) mechanical dispersion [4, 7, 38]

$$\mathbf{D}(\mathbf{u}) = d_m\phi\mathbf{I} + d_t|\mathbf{u}|\mathbf{I} + \frac{d_l - d_t}{|\mathbf{u}|}\begin{pmatrix} u_x^2 & u_xu_y \\ u_xu_y & u_y^2 \end{pmatrix}, \tag{2.5}$$

with d_m being the molecular diffusion coefficient, $\mathbf{I}$ being the 2×2 identity tensor, and d_t and d_l being the transverse and longitudinal dispersivities, respectively.

Like the derivation of Eq. (2.3), we rewrite Eq. (2.4) as a partial differential equation

$$\frac{\partial(\phi\rho c)}{\partial t} + \nabla \cdot (\rho \mathbf{u} c - \rho \mathbf{D}(\mathbf{u}) \nabla c) = q c^*, \qquad \mathbf{x} \in \Omega, \quad t \in (0, T]. \tag{2.6}$$

2.3. Darcy's Law

Darcy's law establishes the basic relationship between the flow rate or the Darcy (superficial) velocity and the pressure gradient, which is the most widely used law or correlation for fluid flows in porous media. Let $p(\mathbf{x}, t)$ be the pressure of the fluid mixture. Darcy's law states

$$\mathbf{u} = -\frac{\mathbf{K}}{\mu(c)}(\nabla p - \rho g \nabla d), \qquad \mathbf{x} \in \Omega, \quad t \in [0, T]. \tag{2.7}$$

Here g is the magnitude of the acceleration due to gravity, $d(\mathbf{x})$ is the depth or elevation of the reservoir, and $\mathbf{K}$ is the permeability tensor of the medium given by

$$\mathbf{K} = \begin{pmatrix} k_{xx}(\mathbf{x}) & k_{xy}(\mathbf{x}) \\ k_{yx}(\mathbf{x}) & k_{yy}(\mathbf{x}) \end{pmatrix}, \tag{2.8}$$

which quantifies the ability of the porous medium to transmit a fluid. In many porous medium flow applications, the permeability tensor $\mathbf{K}$ is a diagonal tensor. Furthermore, the medium is often isotropic; i.e., $k_{xx}(\mathbf{x}) = k_{yy}(\mathbf{x})$. $\mu(c)$ is the viscosity of the fluid mixture, which is concentration-dependent and is often determined by the mixing rule [24]

$$\mu(c) = \mu_0[(1 - c) + M^{1/4} c]^{-4}. \tag{2.9}$$

Here μ_0 is the viscosity of the resident fluid (e.g., oil in petroleum reservoir simulation). The behavior of $\mu(c)$, as a function of c, has an extremely important effect on the efficiency of the displacement process and ultimate oil recovery in petroleum reservoir simulation or the efficiency in the remediation process in environmental modeling. The behavior of $\mu(c)$ in turn depends heavily on the mobility ratio $M = \mu_0/\mu_s = \mu(0)/\mu(1)$, where μ_s is the viscosity of the invading fluid or solvent in petroleum reservoir simulation or that of the solute or solvent in subsurface contaminant transport. If $M > 1$, the displacement process has an adverse mobility ratio and the viscous fingering phenomenon is expected to occur.

2.4. Equations of State

Note that the system of partial differential equations (2.3), (2.6), and (2.7) is underdetermined, since four partial differential equations (note Eq. (2.7) is a vector differential equation of two components involving $\mathbf{u} = (u_x, u_y)$) contain five primary variables (the density ρ, the pressure p, the Darcy velocity $\mathbf{u} = (u_x, u_y)$, and the concentration c of the solute or solvent). Therefore, an additional equation is needed to close the system.

Let V be the specific volume. The compressibility of a fluid c_ρ is defined to be the rate of change of V with respect to the pressure p per unit volume. Mathematically, c_ρ can be

expressed by [43, 52]

$$c_\rho = -\frac{1}{V}\frac{\partial V}{\partial p}, \tag{2.10}$$

where the minus sign in the definition takes into account the fact that the volume V decreases as the pressure p increases. Since the density $\rho = 1/V$, Eq. (2.10) can be rewritten as

$$c_\rho = \frac{1}{\rho}\frac{\partial \rho}{\partial p}. \tag{2.11}$$

For constant c_p, integration of Eq. (2.11) yields an equation of the form

$$\rho = \rho_r \exp(c_\rho(p - p_r)), \tag{2.12}$$

where ρ_r is the reference density at the reference pressure p_r. Equation (2.12) and its simplified versions have been widely used in modeling subsurface contaminant transport and remediation in the hydroscience community. They can also be applied to compressible fluid flow processes in a reservoir simulation, unless the fluids contain large quantities of dissolved gas [38].

Due to the effect of large pressure changes involved in porous medium fluid flow processes and the type of the medium of the reservoir, the porous medium can deform. In this paper we consider the following constitutive relation that has been used very often to model the deformation ϕ [4, 7, 34],

$$\phi = \phi_r(\mathbf{x}) \exp(c_\phi(\mathbf{x})(p - p_r)), \tag{2.13}$$

where $c_\phi(\mathbf{x})$ is the compressibility of the medium and $\phi_r(\mathbf{x})$ is the reference porosity of the medium at the reference pressure p_r. The porosity model (2.13) considers only the volumetric effect of the porous medium deformation caused by the fluid flow process but not vice versa. If the porous medium consists of stress-sensitive elasto-plastic material, more accurate (and possibly more complicated) constitutive relations should be used, which could introduce stronger nonlinearities to the mathematical model through, e.g., the $s_p(\mathbf{x}, p)$ term defined in Eq. (2.15). We refer interested readers to [14, 35] for more details.

2.5. A System of PDEs for Compressible Fluid Flow in Porous Media

After we have derived the governing partial differential equations and equations of state for compressible fluid flows in porous media, we now reformat them into a system of PDEs and constraining equations. Similarly to the mathematical models for incompressible fluid flow [7, 20, 21, 24], we combine the governing equation for the conservation of mass of the fluid mixture (2.3) and Darcy's law (2.7) to form a system of PDEs for the pressure p and the flow rate. But in compressible fluid flow processes, the density ρ of the fluid is not assumed to be constant and cannot be canceled from the governing equation. Hence, the Darcy velocity $\mathbf{u}$ has been used as a primary variable. In the current context, we use the mass flow rate $\boldsymbol{\sigma} = \rho\mathbf{u}$ as a primary variable. We also use Eqs. (2.12) and (2.13) to differentiate the accumulation term in Eq. (2.3) with respect to p, leading to a system of PDEs for the

pressure p and the mass flow rate $\boldsymbol{\sigma}$,

$$\begin{aligned} s_p(\mathbf{x}, p)\frac{\partial p}{\partial t} + \nabla \cdot \boldsymbol{\sigma} &= q, && \mathbf{x} \in \Omega, \quad t \in (0, T], \\ \boldsymbol{\sigma} = \rho \mathbf{u} &= -\frac{\rho(p)\mathbf{K}}{\mu(c)}(\nabla p - \rho(p) g \nabla d), && \mathbf{x} \in \Omega, \quad t \in (0, T], \end{aligned} \tag{2.14}$$

where $s_p(\mathbf{x}, p)$ is the storage term defined by

$$s_p(\mathbf{x}, p) = \frac{\partial(\phi\rho)}{\partial p} = \rho(p)\phi(\mathbf{x}, p)(c_\phi(\mathbf{x}) + c_\rho). \tag{2.15}$$

We can also rewrite the governing equation (2.6) in terms of the mass flow rate $\boldsymbol{\sigma}$ as

$$\frac{\partial(\phi\rho c)}{\partial t} + \nabla \cdot (\boldsymbol{\sigma} c - \mathbf{D}(\boldsymbol{\sigma}, p)\nabla c) = q c^*, \qquad \mathbf{x} \in \Omega, \quad t \in (0, T], \tag{2.16}$$

where the diffusion–dispersion tensor $\mathbf{D}(\boldsymbol{\sigma}, p)$ is defined by

$$\mathbf{D}(\boldsymbol{\sigma}, p) = \rho(p)\mathbf{D}(\mathbf{u}) = d_m \phi(\mathbf{x}, p)\rho(p)\mathbf{I} + d_t|\boldsymbol{\sigma}|\mathbf{I} + \frac{d_l - d_t}{|\boldsymbol{\sigma}|}\begin{pmatrix} \sigma_x^2 & \sigma_x\sigma_y \\ \sigma_x\sigma_y & \sigma_y^2 \end{pmatrix}, \tag{2.17}$$

with $\boldsymbol{\sigma} = (\sigma_x, \sigma_y)$.

Therefore, a mathematical model for describing compressible fluid flows in porous media is described by a system of partial differential equations (2.14) and (2.16), as well as the equations of state (2.12) and (2.13) that provide the constitutive relationship $\rho = \rho(p)$ and $\phi = \phi(\mathbf{x}, p)$. This system also needs to be closed by the initial conditions for the pressure $p(\mathbf{x}, t)$ and the concentration $c(\mathbf{x}, t)$,

$$\begin{aligned} c(\mathbf{x}, 0) &= c_0(\mathbf{x}), && \mathbf{x} \in \Omega, \\ p(\mathbf{x}, 0) &= p_0(\mathbf{x}), && \mathbf{x} \in \Omega, \end{aligned} \tag{2.18}$$

and boundary conditions. In petroleum reservoir simulation the boundary $\partial\Omega$ is typically impermeable, leading to no-flow boundary conditions of the form [38]

$$\begin{aligned} \boldsymbol{\sigma} \cdot \mathbf{n} &= 0, && (\mathbf{x}, t) \in \partial\Omega \times [0, T], \\ \mathbf{D}(\boldsymbol{\sigma}, p)\nabla c) \cdot \mathbf{n} &= 0, && (\mathbf{x}, t) \in \partial\Omega \times [0, T]. \end{aligned} \tag{2.19}$$

These conditions also arise in environmental modeling even though other types of boundary conditions are possible [7]. For simplicity and definiteness of exposition, we consider boundary conditions (2.19) and assume $\Omega = (a_x, b_x) \times (a_y, b_y)$ to be a rectangular domain.

Remark 2.1. The system (2.12)–(2.17) is a strongly coupled system of time-dependent nonlinear partial differential equations and constraining equations. In porous medium fluid flow processes, diffusion or dispersion is often a small phenomenon relative to advection. Moreover, laboratory experiments have found that the longitudinal dispersivity d_l is typically considerably greater than the transverse dispersivity d_t and that the molecular diffusion coefficient d_m is very small by comparison. Hence, Eq. (2.16) is an advection–diffusion equation with advection being the dominant phenomenon. In addition, the effective Peclet number of these problems is large, and sharp traveling interfaces between the injected and

resident fluids diffuse slowly as they move through the reservoir. Finally, the viscosity $\mu(c)$ in Eq. (2.7) changes very rapidly with the concentration in the neighborhood of the moving fluid interface and is fairly constant away from the steep front region. In actual reservoir displacement, the mobility ratio M is usually much larger than 1. Thus, these displacement processes have a large adverse mobility ratio and viscous fingering instability could occur.

Remark 2.2. For an incompressible fluid flow and medium, the density ρ is a constant and $\phi = \phi(\mathbf{x})$ is independent of the pressure p. The system (2.12)–(2.17) is reduced to the model

$$\begin{aligned} \nabla \cdot \mathbf{u} &= \frac{q}{\rho}, && \mathbf{x} \in \Omega, \quad t \in (0, T], \\ \mathbf{u} &= -\frac{\mathbf{K}}{\mu(c)}(\nabla p - \rho g \nabla d), && \mathbf{x} \in \Omega, \quad t \in (0, T], \end{aligned} \tag{2.20}$$

and

$$\phi(\mathbf{x})\frac{\partial c}{\partial t} + \nabla \cdot (\mathbf{u}c - \mathbf{D}(\mathbf{u})\nabla c) = \frac{qc^*}{\rho}, \qquad \mathbf{x} \in \omega, \quad t \in (0, T], \tag{2.21}$$

with $\mathbf{D}(\mathbf{u})$ being given by Eq. (2.5). The system for compressible fluid flows (2.12)–(2.17) has much stronger nonlinearity and couplings, due to the effect of the storage term $s_p(\mathbf{x}, p)$ and Eqs. (2.12)–(2.13).

Remark 2.3. While the system (2.12)–(2.17) and nonlinear hyperbolic conservation laws share such common difficulties as moving steep fronts and advection dominance, they also have salient differences. In aerodynamics, the concerned fluids are mainly gases (air) that are highly compressible. The solutions to these problems often exhibit "shock discontinuities," mainly due to the effect of the nonlinear flux functions and couplings. The interaction of these shock discontinuities can be extremely difficult to model, to analyze, and to simulate. In subsurface porous medium fluid flow processes, the major features and/or difficulties include the nonlinearity and couplings of the differential equations (2.14) and (2.16) as well as the equations of state (2.12) and (2.13), the singularities of the solutions at point sources and sinks, the strong heterogeneity of the porous medium, the compressibility of the fluid mixture and the medium, the large mobility ratio in the displacement processes, and the enormous size of field-scale application and the required long time period of prediction.

3. A MIXED FINITE ELEMENT METHOD FOR THE PRESSURE EQUATION

One important issue in the numerical solution of the system (2.12)–(2.17) is the manner in which the mass flow rate $\boldsymbol{\sigma}$, which governs the basic flow properties of the fluid flow process, is calculated. Since the advection and diffusion–dispersion terms in the transport equation (2.16) are governed by the mass flow rate $\boldsymbol{\sigma}$, accurate simulation to Eq. (2.16) requires an accurate approximation to the mass flow rate $\boldsymbol{\sigma}$. However, the flow properties of the porous media often change abruptly with sharp changes in lithology. Also, as discussed in Section 2.3, the viscosity $\mu(c)$ also changes rapidly in space across steep fluid interfaces. These sharp changes are accompanied by large changes in the pressure gradient ∇p which, in a compensatory fashion, yield a fairly smooth mass flow rate $\boldsymbol{\sigma}$. The standard finite difference and finite element methods solve Eq. (2.14) for the pressure p directly, which may

not be smooth due to the rough coefficients in these PDEs. The pressure p is differentiated and then multiplied by a possibly rough coefficient $\mathbf{K}/\mu$ to determine the mass flow rate $\boldsymbol{\sigma}$ via Eq. (2.14). Therefore, the resulting mass flow rate $\boldsymbol{\sigma}$ is rough and often inaccurate, which then reduces the accuracy of the approximation to the transport equation (2.16).

Mixed finite element methods approximate both p and ∇p from a second-order elliptic PDE simultaneously, yielding accurate approximations to ∇p [5, 11, 30, 42]. Moreover, MFEMs conserve mass, which is of essential importance in these applications. Because of these properties, MFEMs have been successfully applied in the numerical simulation to the system of incompressible fluid flow (2.20)–(2.21) in reservoir simulation for obtaining the pressure p and the Darcy velocity $\mathbf{u}$ simultaneously [19, 26, 47].

3.1. Weak Formulation

Motivated by these results, we apply the MFEM to solve the parabolic pressure equation (2.14) in the system of compressible porous medium fluid flows (2.12)–(2.17) in order to obtain an accurate mass flow rate $\boldsymbol{\sigma}$ as well as the pressure p. Let $L^2(\Omega)$ be the standard function space of all the Lebesgue square integrable functions on Ω. Then we define the Sobolev spaces

$$\begin{aligned} H^1(\Omega) &= \{v(\mathbf{x}) \in L^2(\Omega) \mid \nabla v(\mathbf{x}) \in (L^2(\Omega))^2\}, \\ H(\mathrm{div};\Omega) &= \{\mathbf{v}(\mathbf{x}) \in (L^2(\Omega))^2 \mid \nabla \cdot \mathbf{v} \in L^2(\Omega)\} \\ H_0(\mathrm{div};\Omega) &= \{\mathbf{v}(\mathbf{x}) \in H(\mathrm{div};\Omega) \mid \mathbf{v}(\mathbf{x}) \cdot \mathbf{n}(\mathbf{x}) = 0, \mathbf{x} \in \partial\Omega\}, \end{aligned} \tag{3.1}$$

and

$$L^2(0,T;X) = \{w(\mathbf{x},t) \mid w(\cdot,t)\colon (0,T) \mapsto X, \|w(\cdot,t)\|_X \in L^2(0,T)\}, \tag{3.2}$$

where X is a Sobolev space defined on Ω.

Multiplying the second equation in Eq. (2.14) by $\mu(c)\rho^{-1}(p)\mathbf{K}^{-1}$ yields

$$\frac{\mu(c)}{\rho(p)}\mathbf{K}^{-1}\boldsymbol{\sigma} + \nabla p = \rho(p) g \nabla d, \qquad \mathbf{x} \in \Omega, \quad t \in [0,T], \tag{3.3}$$

where $\mathbf{K}^{-1}$ is the inverse of the permeability tensor. Integrating Eq. (3.3) with any test function $\mathbf{v} \in H_0(\mathrm{div};\Omega)$ applying the divergence theorem to the ∇p term, and then integrating the first equation in Eq. (2.14) against any test functions $w(\mathbf{x}) \in L^2$ we obtain the following weak formulation: Find a pair $(\boldsymbol{\sigma}(\mathbf{x},t),\ p(\mathbf{x},t)) \in L^2(0,T;\ H_0(\mathrm{div};\Omega) \times L^2(\Omega))$ such that

$$\begin{aligned} &\int_\Omega \frac{\mu(c)}{\rho(p)}\mathbf{K}^{-1}\boldsymbol{\sigma} \cdot \mathbf{v}\, d\mathbf{x} - \int_\Omega p \nabla \cdot \mathbf{v}\, d\mathbf{x} = \int_\Omega \rho(p) g \nabla d \cdot \mathbf{v}\, d\mathbf{x}, \\ &\int_\Omega w \nabla \cdot \boldsymbol{\sigma}\, d\mathbf{x} + \int_\Omega s_p(\mathbf{x},p)\frac{\partial p}{\partial t} w\, d\mathbf{x} = \int_\Omega q w\, d\mathbf{x} \\ &\qquad \forall (\mathbf{v}, w) \in H_0(\mathrm{div};\Omega) \times L^2(\Omega), \quad t \in (0,T], \end{aligned} \tag{3.4}$$

with the initial value $p(\mathbf{x},0) = p_0(\mathbf{x})$.

3.2. A Mixed Finite Element Method

Let K and L represent the numbers of grid blocks in the x-direction and the y-direction. We define a spatial partition on the domain $\Omega = (a_x, b_x) \times (a_y, b_y)$,

$$\begin{aligned} a_x = x_0^p < x_1^p < \cdots < x_k^p < \cdots < x_{K-1}^p < x_K^p = b_x, \\ a_y = y_0^p < y_1^p < \cdots < y_l^p < \cdots < y_{L-1}^p < y_L^p = b_y, \end{aligned} \tag{3.5}$$

with $\Delta x_k^p = x_k^p - x_{k-1}^p$ for $k = 1, 2, \ldots, K$ and $\Delta y_l^p = y_l^p - y_{l-1}^p$ for $l = 1, 2, \ldots, L$. We introduce the lowest-order Raviart–Thomas MFEM space on Ω with the partition (3.5)

$$\begin{aligned} S^\sigma(\Omega) &= \left(M_{0,1}^p[a_x, b_x] \times M_{-1,0}^p[a_y, b_y]\right) \times \left(M_{-0,1}^p[a_x, b_x] \times M_{0,1}^p[a_y, b_y]\right), \\ S_0^\sigma(\Omega) &= \{\mathbf{v}(\mathbf{x}) \in S^p(\Omega) \,|\, \mathbf{v}(\mathbf{x}) \cdot \mathbf{n}(\mathbf{x}) = 0, \mathbf{x} \in \partial\Omega\}, \\ S^p(\Omega) &= M_{-1,0}^p[a_x, b_x] \times M_{-1,0}^p[a_y, b_y], \end{aligned} \tag{3.6}$$

with

$$\begin{aligned} M_{\alpha,\beta}^p[a_x, b_x] &= \left\{v(x) \in C^\alpha[a_x, b_x] \,|\, v(x) \in P_\beta\left[x_{k-1}^p, x_k^p\right],\ k = 1, 2, \ldots, K\right\}, \\ M_{\alpha,\beta}^p[a_y, b_y] &= \left\{v(x) \in C^\alpha[a_y, b_y] \,|\, v(x) \in P_\beta\left[y_{l-1}^p, y_l^p\right],\ l = 1, 2, \ldots, L\right\}. \end{aligned} \tag{3.7}$$

Here $C^0[a, b]$ and $C^{-1}[a, b]$ are the spaces of continuous and piecewise continuous functions, respectively. P_β is the space of univariate polynomials of degree less than or equal to β.

In the numerical simulation for the system (2.12)–(2.17), we use a time stepping procedure. Let N be the number of time steps on the interval $[0, T]$; we define a temporal partition by

$$0 = t_0 < t_1 < \cdots < t_n < \cdots < t_{N-1} < t_N = T, \tag{3.8}$$

with $\Delta t_n = t_n - t_{n-1}$ for $n = 1, 2, \ldots, N$.

A fully discrete mixed finite element method for the pressure equation (2.14) reads as follows: For $n = 1, 2, \ldots, N$, find a pair $(\boldsymbol{\sigma}_h(\mathbf{x}, t_n),\ p_h(\mathbf{x}, t_n)) \in S_0^\sigma(\Omega) \times S^p(\Omega)$, such that

$$\begin{aligned} &\int_\Omega \frac{\mu(c(\cdot, t_n))}{\rho(\overline{p}_h(\cdot, t_n))} \mathbf{K}^{-1} \boldsymbol{\sigma}_h(\cdot, t_n) \cdot \mathbf{v}_h \, d\mathbf{x} - \int_\Omega p_h(\cdot, t_n) \nabla \cdot \mathbf{v}_h \, d\mathbf{x} \\ &\quad = \int_\Omega \rho(\overline{p}_h(\cdot, t_n)) g \nabla d \cdot \mathbf{v}_h \, d\mathbf{x}, \\ &\Delta t_n \int_\Omega w_h \nabla \cdot \boldsymbol{\sigma}_h(\cdot, t_n) \, d\mathbf{x} + \int_\Omega s_p(\overline{p}_h(\cdot, t_n)) p_h(\cdot, t_{n-1}) w_h \, d\mathbf{x} \\ &\quad = \Delta t_n \int_\Omega q(\cdot, t_n) w_h \, d\mathbf{x} + \int_\Omega s_p(\overline{p}_h(\cdot, t_n)) p_h(\cdot, t_{n-1}) w_h \, d\mathbf{x}, \\ &\qquad \forall (\mathbf{v}_h, w_h) \in S_0^\sigma(\Omega) \times S^p(\Omega), \end{aligned} \tag{3.9}$$

with $p_h(\mathbf{x}, 0) \in S^p(\Omega)$ being an approximation to $p_0(\mathbf{x})$. Here $c(\mathbf{x}, t_n)$ is assumed known and $\overline{p}_h(\mathbf{x}, t_n)$ is a projected value of $p_h(\mathrm{x}, t_n)$. The details will be presented in Section 5, in which we present a decoupling and linearization technique for system (2.12)–(2.17).

Remark 3.1. Besides the standard advantages of the MFEM mentioned at the beginning of this section, the Raviart–Thomas expression of the mass flow rate $\boldsymbol{\sigma}(\mathbf{x}, t_n)$ is particularly well-suited for the semi-analytical characteristic tracking used in the ELLAM scheme for the transport equation (2.16). In addition, the characteristic tracking in the MMOC scheme [22, 27, 45] often runs out of the physical domain Ω numerically and causes implementational and analytical problems. These problems have been treated in an *ad hoc* manner in the MMOC simulation and remain a troublesome issue. In contrast, because the no-flow boundary condition (the first equation in Eq. (2.19)) is treated as an essential boundary condition in the MFEM (3.9), the semi-analytical characteristic tracking in the ELLAM scheme is naturally guaranteed not to flow out of the physical domain Ω. This is an additional advantage of the MFEMs when they are combined with the ELLAM scheme.

Remark 3.2. MFEMs reformulate the parabolic pressure equation (2.14) as a first-order system of PDEs. This system is more complicated to solve than that of a standard FDM or FEM. Also, the MFEM trial and test function spaces for p and $\boldsymbol{\sigma}$ must be chosen carefully, so that they satisfy the inf-sup stability condition. Extensive research has been conducted on the efficient solution of the MFEM system [2, 3, 10, 12, 36]. Finally, an additional numerical difficulty for MFEMs in subsurface porous medium fluid flows is the effect of the singular source and sink terms $q(\mathbf{x}, t)$ as well as the discontinuous coefficients. Related studies can be found in the references mentioned and in [19, 26, 47].

4. AN ELLAM SCHEME FOR THE TRANSPORT EQUATION

In this section, we develop an ELLAM scheme for the transport equation (2.16) with the assumption that the pressure p and the mass flow rate $\boldsymbol{\sigma}$ are known.

4.1. A Reference Equation

The ELLAM scheme uses a time-marching algorithm, so we only need to concentrate on the current time interval $[t_{n-1}, t_n]$ defined by (3.8). Multiplying the advection-diffusion transport equation (2.16) by space-time test functions $z(\mathbf{x}, t)$ that are continuous and piecewise smooth, vanish outside the space-time strip $\Omega \times (t_{n-1}, t_n]$, and are discontinuous in time at time t_{n-1}, we come up with a space-time weak formulation for Eq. (2.16):

$$\begin{aligned}
&\int_\Omega \phi\rho\, c(\mathbf{x}, t_n) z(\mathbf{x}, t_n)\, d\mathbf{x} + \int_{t_{n-1}}^{t_n} \int_\Omega \nabla z(\mathbf{y}, \theta) \cdot \mathbf{D}(\boldsymbol{\sigma}, p) \nabla c(\mathbf{y}, \theta)\, d\mathbf{y}\, d\theta \\
&\quad - \int_{t_{n-1}}^{t_n} \int_\Omega c(\mathbf{y}, \theta) \left[\phi\rho \frac{\partial z(\mathbf{y}, \theta)}{\partial \theta} + \boldsymbol{\sigma} \cdot \nabla z(\mathbf{y}, \theta) \right] d\mathbf{y}\, d\theta \\
&\quad = \int_\Omega \phi\rho c(\mathbf{x}, t_{n-1} z(\mathbf{x}, t_{n-1}^+)\, d\mathbf{x} + \int_{t_{n-1}}^{t_n} \int_\Omega c^* q z(\mathbf{y}, \theta)\, d\mathbf{y}\, d\theta. \qquad (4.1)
\end{aligned}$$

Here $z(\mathbf{x}, t_{n-1}^+ = \lim_{t \to t_{n-1}, t > t_{n-1}} z(\mathbf{x}, t)$ to take into account the fact that $z(\mathbf{x}, t)$ is discontinuous in time at time t_{n-1}. For simplicity of notations, we do not explicitly express the dependence of $\rho = \rho(p)$, $\phi = \phi(\mathbf{x}, p)$, and $\boldsymbol{\sigma} = \sigma(\mathbf{x}, t)$ on $\mathbf{x}$, t, and p. The dependence should be fairly clear from the context.

In the ELLAM framework [13, 33], an appropriate operator splitting of the adjoint equation of Eq. (2.16) concludes that the test functions $z(\mathbf{y}, \theta)$ should be chosen to satisfy the

hyperbolic part of the adjoint equation of Eq. (2.16)

$$\phi\rho\frac{\partial z}{\partial\theta}(\mathbf{y},\theta)+\boldsymbol{\sigma}\cdot\nabla z(\mathbf{y},\theta)=0,\qquad \mathbf{y}\in\Omega,\quad \theta\in[t_{n-1},t_n]. \tag{4.2}$$

Thus, the test functions $z(\mathbf{y},\theta)$ should be constant along the characteristics $\mathbf{y}=\mathbf{r}(\theta;\mathbf{x},t_n)$ defined by the initial-value problem of the ordinary differential equation (ODE)

$$\begin{aligned}\frac{d\mathbf{r}}{d\theta}&=\frac{\sigma}{\phi\rho},\qquad \theta\in[t_{n-1},t_n],\\ \mathbf{r}(\theta;\mathbf{x},t)|_{\theta=t}&=\mathbf{x}.\end{aligned} \tag{4.3}$$

For any $(\mathbf{y},\ \theta)\in\Omega\times[t_{n-1},t_n]$, there exists an $\mathbf{x}\in\Omega$ such that $\mathbf{y}=\mathbf{r}(\theta;\mathbf{x},t_n)$. We use the Euler method to evaluate the second (source) term on the right-hand side of Eq. (4.1) to get

$$\begin{aligned}&\int_{t_{n-1}}^{t_n}\int_\Omega (c^*q)(\mathbf{y},\theta)z(\mathbf{y},\theta)\,d\mathbf{y}\,d\theta\\ &\quad=\int_\Omega\int_{t_{n-1}}^{t_n}(c^*q)(\mathbf{r}(\theta;\mathbf{x},t_n)\theta))z(\mathbf{x},t_n)|\mathbf{J}(\theta;x,t_n)|\,d\theta\,d\mathbf{x}\\ &\quad=\Delta t_n\int_\Omega c^*(\mathbf{x},t_n)q(\mathbf{x},t_n)z(\mathbf{x},t_n)\,d\mathbf{x}+E_q(c^*,z),\end{aligned} \tag{4.4}$$

where

$$|\mathbf{J}(\theta;\mathbf{x},t_n)|=\left|\frac{\partial\mathbf{r}(\theta;\mathbf{x},t_n)}{\partial\mathbf{x}}\right|=1+\mathcal{O}(t_n-\theta) \tag{4.5}$$

is the Jacobian of the transformation from $\mathbf{x}$ to $\mathbf{r}(\theta;\mathbf{x},t_n)$, and $E_q(c^*,z)$ is the truncation error due to the application of the Euler quadrature.

Similarly, we can evaluate the diffusion–dispersion term and have

$$\begin{aligned}&\int_{t_{n-1}}^{t_n}\int_\Omega\nabla z(\mathbf{y},\theta)\cdot\mathbf{D}(\boldsymbol{\sigma},\ p)\nabla c(\mathbf{y},\theta)\,d\mathbf{y}\,d\theta\\ &\quad=\Delta t_n\int_\Omega\nabla z(\mathbf{x},t_n)\cdot\mathbf{D}(\boldsymbol{\sigma},\ p)\nabla c(\mathbf{x},t_n)\,d\mathbf{x}+E_{\mathbf{D}}(c,z),\end{aligned} \tag{4.6}$$

where $E_{\mathbf{D}}(c,z)$ is the truncation error term.

Substituting Eqs. (4.4) and (4.6) into Eq. (4.1), we obtain a reference equation for the transport equation (2.16),

$$\begin{aligned}&\int_\Omega\phi(\mathbf{x},\ p(\mathbf{x},t_n))\rho(p(\mathbf{x},t_n))c(\mathbf{x},t_n)z(\mathbf{x},t_n)\,d\mathbf{x}\\ &\qquad+\Delta t_n\int_\Omega\nabla z(\mathbf{x},t_n)\cdot\mathbf{D}(\boldsymbol{\sigma}(\mathbf{x},t_n),\ p(\mathbf{x},t_n))\nabla c(\mathbf{x},t_n)\,d\mathbf{x}\\ &\quad=\int_\Omega\phi(\mathbf{x},\ p(\mathbf{x},t_{n-1}))\rho(p(\mathbf{x},t_{n-1}))c(\mathbf{x},t_{n-1})z(\mathbf{x},t_{n-1}^+)\,d\mathbf{x}\\ &\qquad-\Delta t_n\int_\Omega c^*(\mathbf{x},t_n)q(\mathbf{x},t_n)z(\mathbf{x},t_n)\,d\mathbf{x}+E(c,z),\end{aligned} \tag{4.7}$$

with

$$E(c,z)=\int_{t_{n-1}}^{t_n}\int_\Omega c(\mathbf{y},\theta)\left[(\phi\rho)\frac{\partial z(\mathbf{y},\theta)}{\partial\theta}+\boldsymbol{\sigma}\cdot\nabla z(\mathbf{y},\theta)\right]d\mathbf{y}\,d\theta + E_{\mathbf{D}}(c,z)-E_q(c^*,z). \tag{4.8}$$

4.2. An ELLAM Scheme

We derive an ELLAM scheme for the transport equation (2.16), based on the reference equation (4.7). Let I and J be the numbers of grid blocks in the x and y directions, respectively. We define a spatial partition on $\Omega=(a_x,b_x)\times(a_y,b_y)$ as

$$\begin{aligned} a_x &= x_0^c<x_1^c<\cdots<x_i^c<\cdots<x_{I-1}^c<x_I^c=b_x,\\ a_y &= y_0^c<y_1^c<\cdots<y_j^c<\cdots<y_{J-1}^c<y_J^c=b_y, \end{aligned} \tag{4.9}$$

with $\Delta x_i^c=x_i^c-x_{i-1}^c$ for $i=1,2,\ldots,I$, and $\Delta y_j^c=y_j^c-y_{j-1}^c$ for $j=1,2,\ldots,J$. The spatial partition (4.9) does not necessarily have to be the same as the spatial partition (3.5) for the pressure equation.

We define the trial and test function spaces to be the space of continuous and piecewise bilinear polynomials on Ω with the spatial partition (4.9)

$$S^c(\Omega)=M_1^c[a_x,b_z]\times M_1^c[a_y,b_y], \tag{4.10}$$

where

$$\begin{aligned} M_1^c[a_x,b_x] &= \left\{v(x)\in C^0[a_x,b_x]\,|\,v(x)\in P_1\left[x_{i-1}^c,x_i^c\right],\ i=1,2,\ldots,I\right\},\\ M_1^c[a_y,b_y] &= \left\{v(x)\in C^0[a_y,b_y]\,|\,v(x)\in P_1\left[y_{j-1}^c,y_j^c\right],\ j=1,2,\ldots,J\right\}. \end{aligned} \tag{4.11}$$

Here $C^0[a,b]$ is the space of continuous functions and P_1 is the space of linear functions.

Under the assumption that the pressure $p_h(\mathbf{x},t_n)$ and the mass flow rate $\boldsymbol{\sigma}_h(\mathbf{x},t_n)$ in Eq. (2.16) are known, the ELLAM scheme can be defined as follows: For $n=1,2,\ldots,N$, find $c_h(\mathbf{x},t_n)\in S^c(\Omega)$ such that

$$\begin{aligned} &\int_\Omega \phi(\mathbf{x},p_h(\mathbf{x},t_n))\rho(p_h(\mathbf{x},t_n))c_h(\mathbf{x},t_n)z(\mathbf{x},t_n)\,d\mathbf{x}\\ &\quad+\Delta t_n\int_\Omega \nabla z_h(\mathbf{x},t_n)\cdot\mathbf{D}(\boldsymbol{\sigma}_h(\mathbf{x},t_n),p_h(\mathbf{x},t_n))\nabla c_h(\mathbf{x},t_n)\,d\mathbf{x}\\ &=\int_\Omega \phi(\mathbf{x},p_h(\mathbf{x},t_{n-1}))\rho(p_h(\mathbf{x},t_{n-1}))c_h(\mathbf{x},t_{n-1})z_h(\mathbf{x},t_{n-1}^+)\,d\mathbf{x}\\ &\quad-\Delta t_n\int_\Omega c^*(\mathbf{x},t_n)q(\mathbf{x},t_n)z_h(\mathbf{x},t_n)\,dx \qquad \forall z_h(\mathbf{x},t_n)\in S^c(\Omega), \end{aligned} \tag{4.12}$$

with $c_h(\mathbf{x},0)\in S^c(\Omega)$ being an approximation to $c_0(\mathbf{x})$.

Remark 4.1. First, by using a characteristic tracking, the ELLAM scheme (4.12) significantly reduces the temporal truncation errors and generates accurate numerical solutions even if very large time steps are used. Second, the ELLAM scheme conserves mass [13, 33], which is of essential importance in applications. Third, the ELLAM scheme (4.12) symmetrizes the governing transport PDE (2.16) and generates a nine-banded, symmetric and positive definite coefficient matrix, which is identical to the coefficient matrix for

parabolic equations discretized by a standard finite element method. Finally, the authors previously performed extensive numerical experiments for one- and two-dimensional linear transport equations, which show that ELLAM schemes often outperform many widely used and well-received numerical methods [1, 56]. Note that once the pressure p and the mass flow rate $\boldsymbol{\sigma}$ are known, the transport equation (2.16) is, in principle, a linear advection–diffusion transport PDE. Hence, we anticipate that the ELLAM scheme (4.12) will generate accurate numerical solutions for the system (2.12)–(2.17). In Section 6, we will perform the numerical experiments to observe the performance of the ELLAM scheme.

Remark 4.2. In the ELLAM scheme (4.12), $c_h(\mathbf{x}, t_n) \in S^c(\Omega)$ and $z_h(\mathbf{x}, t_n) \in S^c(\Omega)$ are piecewise-bilinear functions at time t_n. Hence, all the terms but the first one on the right-hand side in Eq. (4.12) are standard integrals for finite element methods and can be evaluated by standard methods. In the first term, the value of $c_h(\mathbf{x}, t_{n-1})$ is known for the solution at the previous time step t_{n-1}. But the test function $z_h(\mathbf{x}, t_{n-1}^+) = \lim_{t \to t_{n-1}, t > t_{n-1}} z_h(\mathbf{x}, t) = z_h(\mathbf{x}^*, t)$, with $x^* = \mathbf{r}(t_n; \mathbf{x}, t_{n-1})$ being the point at the head of the characteristic that corresponds to $\mathbf{x}$ at the foot. The evaluation of this term is a very challenging issue, due to the deformation of each cell $[x_{i-1}^c, x_i^c] \times [y_{j-1}^c, y_j^c]$ on which the test functions are defined as the geometry is backtracked from time step t_n to time step t_{n-1}. The most practical approach for evaluating this term is to use a forward-tracking algorithm [46]. This would enforce an integration quadrature at time step t_{n-1} with respect to the fixed spatial grids (4.9) on which $c(\mathbf{x}, t_{n-1})$ is defined. The evaluation of the test function $z(\mathbf{x}, t_{n-1}^+)$ is difficult. Rather than backtracking the geometry and estimating the test functions by mapping the deformed geometry onto the fixed grids (4.9), we will forward track discrete quadrature points chosen on the fixed grid at the time step t_{n-1} to time step t_n, where evaluation of $z_h(\mathbf{x}, t)$ is straight forward. Notice that this forward tracking has no effect on the solution grid (4.9) or the data structure of the scheme (4.12). Therefore, this forward-tracking algorithm avoids the complication of distorted grids of previous forward-tracking methods or the complication of backtracking geometry of backtracking methods.

Remark 4.3. For a general mass flow rate field $\boldsymbol{\sigma}(\mathbf{x}, t)$, porosity $\phi(\mathbf{x}, p)$ and density $\rho(p)$, one cannot analytically solve the initial-value problem (4.9) to track the characteristics. Hence, numerical means have to be used to approximate the characteristics. In the context of linear transport PDEs where the fluid velocity is assumed to be a known smooth function, we were able to utilize Euler quadrature or a Runge–Kutta quadrature to track characteristics and to obtain accurate numerical solutions [56]. However, in the ELLAM scheme (4.12), the mass flow rate $\boldsymbol{\sigma}(\mathbf{x}, t_n)$ is given as a Raviart–Thomas solution to the pressure equation (2.14). Thus, the Euler and Runge–Kutta methods used in [56] and virtually all quadratures based on the numerical solutions of ordinary differential equations with smooth right-hand sides could introduce fairly large errors to the characteristic tracking procedure. These errors in turn affect the accuracy of the numerical solutions of ELLAM schemes.

Note that in applications the porosity ϕ and ρ are constant on each cell and that the flow rate $\boldsymbol{\sigma}_h$ is a Raviart–Thomas solution. Therefore, we can analytically solve a modified initial-value problem

$$\begin{aligned} \frac{d\mathbf{r}}{d\theta} &= \frac{\boldsymbol{\sigma}_h(\mathbf{x}, t_n)}{\phi(\mathbf{x}, p_h(\mathbf{x}, t_n))\rho(p_h(\mathbf{x}, t_n))}, \qquad \theta \in [t_{n-1}, t_n], \\ \mathbf{r}(\theta; \mathbf{x}, t)|_{\theta=t} &= \mathbf{x} \end{aligned} \tag{4.13}$$

on each cell to track the characteristics on a cell-by-cell basis [32, 40, 48]. In this approach, we significantly improve the accuracy of the characteristic tracking and greatly minimize the effect of the point source and sink singularities on the characteristic tracking. Furthermore, because the mass flow rate $\boldsymbol{\sigma}$ exactly satisfies the no-flow boundary condition (2.19) due to its treatment as an essential boundary condition in the MFEM scheme (3.9), the characteristic tracking determined by Eq. (4.13) never runs out of the physical domain Ω and avoids the loss of mass in the ELLAM scheme (4.12). This is another advantage of the ELLAM scheme when applied to the system (2.12)–(2.17).

5. AN ELLAM-MFEM SOLUTION TECHNIQUE FOR SYSTEMS OF COMPRESSIBLE FLUID FLOWS IN POROUS MEDIA

In this section, we develop an ELLAM-MFEM sequential solution technique for systems of compressible fluid flows in porous media, which are given by Eqs. (2.12)–(2.17). As we discussed in Remarks 2.1–2.3, the numerical simulation of these systems encounters serious difficulties and complexities, including the advection dominance of the advection–diffusion transport PDE (2.16) and the moving steep fronts present in its solutions, the nonlinearity and close couplings between the equations in the system, the singularities of the solutions at point sources and sinks, the strong heterogeneity of the porous medium, the compressibility of the fluid mixture and the medium, the large mobility ratio in displacement processes, the enormous size of field-scale application, and the required long time period of prediction. A blind linearization with little regard to the properties of the equations or the solutions can result in extremely large, ill-conditioned, nonlinear systems. The accurate solution of these equations can be extremely difficult and expensive. These issues, if not treated carefully, may destroy the usefulness of the simulation. Fully coupled and fully implicit methods, which solve all of the coupled nonlinear PDEs in an implicit fashion and which have been widely used in large-scale simulators in industry, are very stable and robust even if large time steps are used in a simulation. But they are fairly expensive to solve per time step and are very diffusive. Because of the effect of the strong temporal errors, the time steps must still be restricted in size, not due to the stability restriction but for the purpose of accuracy of a simulation.

In this section, we develop an ELLAM-MFEM sequential solution technique for system (2.12)–(2.17), in which we use the ELLAM scheme (4.12) to solve the transport equation (2.16) and the mixed finite element method (3.9) to solve the pressure equation (2.14). Notice that in subsurface porous medium fluid flow processes, the mass flow rate $\boldsymbol{\sigma}$ is fairly smooth outside neighborhoods of the point sources and sinks. Therefore, we allow the use of coarser spatial grids (3.5) for the pressure equation (2.14) than the spatial grids (4.9) for the transport equation (2.16).

To derive an ELLAM-MFEM iterative solution procedure, we define the following approximations to the pressure $p_h(\mathbf{x}, t_n)$, the mass flow rate $\boldsymbol{\sigma}_h(\mathbf{x}, t_n)$, and the concentration $c_h(\mathbf{x}, t_n)$ by using extrapolation operators

$$E_1 f(\mathbf{x}, t_n) = f(\mathbf{x}, t_{n-1}), \qquad n = 1, 2, \ldots, N, \tag{5.1}$$

and

$$E_2 f(\mathbf{x}, t_n) = \begin{cases} f(\mathbf{x}, t_{n-1}), & n = 1, \\ \left(1 + \frac{\Delta t_n}{\Delta t_{n-1}}\right) f(\mathbf{x}, t_{n-1}) - \frac{\Delta t_n}{\Delta t_{n-1}} f(\mathbf{x}, t_{n-2}), & n = 2, 3, \ldots, N. \end{cases} \tag{5.2}$$

Here f could be the pressure p_h or the concentration c_h.

Recalling the hyperbolic nature of the transport equation (2.16), we can also define an extrapolation along the characteristics for the concentration c_h,

$$E_3 c_h(\mathbf{x}, t_n) = c_h(\mathbf{x}^*, t_{n-1}), \qquad n = 1, 2, \ldots, N. \tag{5.3}$$

where $\mathbf{x}^*$ is the foot of the characteristic $\mathbf{x}^* = r(t_{n-1}; \mathbf{x}, t_n)$ defined by the ODE

$$\begin{aligned} \frac{d\mathbf{r}}{d\theta} &= \frac{\boldsymbol{\sigma}_h(\mathbf{x}, t_{n-1})}{\phi(\mathbf{x}, p_h(\mathbf{x}, t_{n-1}))\rho(p_h(\mathbf{x}, t_{n-1}))}, \qquad \theta \in [t_{n-1}, t_n], \\ \mathbf{r}(\theta; \mathbf{x}, t_n)|_{\theta = t_n} &= \mathbf{x}. \end{aligned} \tag{5.4}$$

We next define a weighted iteration operator F_ω by

$$F_\omega f^{(m)}(\mathbf{x}, t_n) = \begin{cases} f^{(0)}(\mathbf{x}, t_n), & m = 1 \\ (1-\omega) f^{(m-2)}(\mathbf{x}, t_n) + \omega f^{(m-1)}(\mathbf{x}, t_n), & m \geq 2. \end{cases} \tag{5.5}$$

where $0 < \omega < 2$ is a weighting parameter for the iterative procedure. $f^{(m)}$ could be $p_h^{(m)}$ or $c_h^{(m)}$ defined in the ELLAM-MFEM solution procedure below.

With these notations introduced, we now define an ELLAM-MFEM iterative sequential solution procedure for systems of compressible fluid flows in porous media, which are defined by Eqs. (2.12)–(2.17), as follows:

A. Initialization: $n = 0$

A1: Define $(p_h(\mathbf{x}, 0), \boldsymbol{\sigma}_h(\mathbf{x}, 0)) \in S^\sigma(\Omega) \times S^p(\Omega)$ by a stationary analogue of Eq. (3.9)

$$\begin{aligned} \int_\Omega \frac{\mu(c_0(\cdot))}{\rho(p_0(\cdot))} \mathbf{K}^{-1}(\boldsymbol{\sigma}_h(\cdot, 0) - \boldsymbol{\sigma}_0(\cdot)) \cdot \mathbf{v}_h \, d\mathbf{x} - \int_\Omega (p_h(\cdot, 0) - p_0(\cdot)) \nabla \cdot \mathbf{v}_h \, d\mathbf{x} = 0, \\ \int_\Omega w_h \nabla \cdot (\boldsymbol{\sigma}_h(\cdot, 0) - \boldsymbol{\sigma}_0(\cdot)) \, d\mathbf{x} = 0, \qquad \forall (\mathbf{v}_h, w_h) \in S_0^\sigma(\Omega) \times S^p(\Omega), \end{aligned} \tag{5.6}$$

with

$$\boldsymbol{\sigma}_0(\mathbf{x}) = -\frac{\rho(p_0(\mathbf{x}))\mathbf{K}}{\mu(c_0(\mathbf{x}))}(\nabla p_0(\mathbf{x}) - \rho(p_0(\mathbf{x}))g\nabla d), \qquad \mathbf{x} \in \Omega, \quad t \in (0, T]. \tag{5.7}$$

In the MFEM scheme (5.6), the pressure $p_h(\mathbf{x}, 0)$ can be determined up to an arbitrary constant. Unlike the numerical simulation to incompressible fluid flows (2.20)–(2.21), where the additional constant in the pressure p_h does not affect the solution procedure at all, in the current context the additional constant in the pressure p_h affects both Eqs. (2.14) and (2.16). To uniquely determine the pressure $p_h(\mathbf{x}, 0)$ while maintaining the conservation of mass, we impose the condition

$$\int_\Omega p_h(\cdot, 0) \, d\mathbf{x} = \int_\Omega p_0(\cdot) \, d\mathbf{x}. \tag{5.8}$$

A2: Define $c_h(\mathbf{x}, 0) \in S^c(\Omega)$ to be the L^2-projection of $c_0(\mathbf{x})$, which is given in Eq. (2.18)

$$\int_\Omega c_h(\cdot, 0) z_h \, d\mathbf{x} = \int_\Omega c_0(\cdot) z_h(\cdot) \, d\mathbf{x}, \qquad \forall z_h \in S^c(\Omega). \tag{5.9}$$

B. Time Stepping Procedure:
for $n = 1, 2, \ldots, N$ **do**

B1. Projection Step:

A. Find the solution pair $(p_h^{(0)}(\mathbf{x}, t_n), \boldsymbol{\sigma}_h^{(0)}(\mathbf{x}, t_n)) \in S^\sigma(\Omega) \times S^p(\Omega)$ such that

$$\begin{aligned}
&\int_\Omega \frac{\mu(Ec_h(\cdot, t_n))}{\rho(Ep_h(\cdot, t_n))} \mathbf{K}^{-1} \boldsymbol{\sigma}_h^{(0)}(\cdot, t_n) \cdot \mathbf{v}_h \, d\mathbf{x} - \int_\Omega p_h^{(0)}(\cdot, t_n) \nabla \cdot \mathbf{v}_h \, d\mathbf{x} \\
&\quad = \int_\Omega \rho(Ep_h(\cdot, t_n)) g \nabla d \cdot \mathbf{v}_h \, d\mathbf{x}, \\
&\Delta t_n \int_\Omega w_h \nabla \cdot \boldsymbol{\sigma}_h^{(0)}(\cdot, t_n) \, d\mathbf{x} + \int_\Omega s_p(Ep_h(\cdot, t_n)) p_h^{(0)}(\cdot, t_n) w_h \, d\mathbf{x} \\
&\quad = \Delta t_n \int_\Omega q(\cdot, t_n) w_h \, d\mathbf{x} + \int_\Omega s_p(Ep_h(\cdot, t_n)) p_h^{(0)}(\cdot, t_{n-1}) w_h \, d\mathbf{x}, \\
&\qquad \forall (\mathbf{v}_h, w_h) \in S_0^\sigma(\Omega) \times S^p(\Omega).
\end{aligned} \tag{5.10}$$

In Eq. (5.10), $Ep_h(\mathbf{x}, t_n)$ could be either $E_1 p_h(\mathbf{x}, t_n)$ or $E_2 p_h(\mathbf{x}, t_n)$ that are defined in Eqs. (5.1) or (5.2). $Ec_h(\mathbf{x}, t_n)$ could be one of the $E_1 c_h(\mathbf{x}, t_n)$, $E_2 c_h(\mathbf{x}, t_n)$, and $E_3 c_h(\mathbf{x}, t_n)$ that are defined in Eqs. (5.1)–(5.3).

B. Find the solution $c_h^{(0)}(\mathbf{x}, t_n) \in S^c(\Omega)$ such that

$$\begin{aligned}
&\int_\Omega \phi\big(\cdot, p_h^{(0)}(\cdot, t_n)\big) \rho\big(p_h^{(0)}(\cdot, t_n)\big) c_h^{(0)}(\cdot, t_n) z_h(\cdot, t_n) \, d\mathbf{x} \\
&\qquad + \Delta t_n \int_\Omega \nabla z_h(\cdot, t_n) \cdot \mathbf{D}\big(\boldsymbol{\sigma}_h^{(0)}(\cdot, t_n), p_h^{(0)}(\cdot, t_n)\big) \nabla c_h(\cdot, t_n) \, d\mathbf{x} \\
&\quad = \int_\Omega \phi(\cdot, p_h(\cdot, t_{n-1})) \rho(p_h(\cdot, t_{n-1})) c_h(\cdot, t_{n-1}) z_h(\cdot, t_{n-1}^+) \, d\mathbf{x} \\
&\qquad - \Delta t_n \int_\Omega c^*(\cdot, t_n) q(\cdot, t_n) z_h(\cdot, t_n) \, d\mathbf{x}, \qquad \forall z_h(\cdot, t_n) \in S^c(\Omega),
\end{aligned} \tag{5.11}$$

To evaluate $z_h(\mathbf{x}, t_{n-1}^+)$, we define a characteristic $\mathbf{r}(\theta; \mathbf{x}, t_{n-1})$ by

$$\begin{aligned}
&\frac{d\mathbf{r}}{d\theta} = \frac{\boldsymbol{\sigma}_h^{(0)}(\mathbf{x}, t_n)}{\phi\big(\mathbf{x}, p_h^{(0)}(\mathbf{x}, t_n)\big) \rho\big(p_h^{(0)}(\mathbf{x}, t_n)\big)}, \qquad \theta \in [t_{n-1}, t_n], \\
&\mathbf{r}(\theta; \mathbf{x}, t_{n-1})|_{\theta = t_{n-1}} = \mathbf{x}.
\end{aligned} \tag{5.12}$$

Then we evaluate $z_h(\mathbf{x}, t_{n-1}^+) = z_h(\tilde{\mathbf{x}}, t_n)$ with $\tilde{\mathbf{x}} = \mathbf{r}(t_n; \mathbf{x}, t_{n-1})$.

B2. Iteration Step:

if ERROR > TOLERANCE **then**

$m = m + 1$.

A. Find the solution pair $(p_h^{(m)}(\mathbf{x}, t_n), \sigma_h^{(m)}(\mathbf{x}, t_n)) \in S^{\sigma}(\Omega) \times S^{p}(\Omega)$ such that

$$\begin{aligned}
&\int_{\Omega} \frac{\mu\big(F_{\omega} c_h^{(m)}(\cdot, t_n)\big)}{\rho\big(F_{\omega} p_h^{(m)}(\cdot, t_n)\big)} \mathbf{K}^{-1} \boldsymbol{\sigma}_h^{(m)}(\cdot, t_n) \cdot \mathbf{v}_h \, d\mathbf{x} - \int_{\Omega} p_h^{(m)}(\cdot, t_n) \nabla \cdot \mathbf{v}_h \, d\mathbf{x} \\
&\quad = \int_{\Omega} \rho\big(F_{\omega} p_h^{(m)}(\cdot, t_n)\big) g \nabla d \cdot \mathbf{v}_h \, d\mathbf{x}, \\
&\Delta t_n \int_{\Omega} w_h \nabla \cdot \boldsymbol{\sigma}_h^{(m)}(\cdot, t_n) \, d\mathbf{x} + \int_{\Omega} s_p\big(F_{\omega} p_h^{(m)}(\cdot, t_n)\big) p_h^{(m)}(\cdot, t_n) w_h \, d\mathbf{x} \\
&\quad = \Delta t_n \int_{\Omega} q(\cdot, t_n) w_h \, d\mathbf{x} + \int_{\Omega} s_p\big(F_{\omega} p_h^{(m)}(\cdot, t_n)\big) p_h^{(m)}(\cdot, t_{n-1}) w_h \, d\mathbf{x}, \\
&\qquad \forall (\mathbf{v}_h, w_h) \in S_0^{\sigma}(\Omega) \times S^{p}(\Omega).
\end{aligned} \tag{5.13}$$

B. Find the solution $c_h^{(m)}(\mathbf{x}, t_n) \in S^{c}(\Omega)$ such that

$$\begin{aligned}
&\int_{\Omega} \phi\big(\cdot, p_h^{(m)}(\cdot, t_n)\big) \rho\big(p_h^{(m)}(\cdot, t_n)\big) c_h^{(m)}(\cdot, t_n) z_h(\cdot, t_n) \, d\mathbf{x} \\
&\qquad + \Delta t_n \int_{\Omega} \nabla z_h(\cdot, t_n) \cdot \mathbf{D}\big(\boldsymbol{\sigma}_h^{(m)}(\cdot, t_n), p_h^{(m)}(\cdot, t_n)\big) \nabla c_h^{(m)}(\cdot, t_n) \, d\mathbf{x} \\
&\quad = \int_{\Omega} \phi(\cdot, p_h(\cdot, t_{n-1})) \rho(p_h(\cdot, t_{n-1})) c_h(\cdot, t_{n-1}) z_h(\cdot, t_{n-1}^{+}) \, d\mathbf{x} \\
&\qquad - \Delta t_n \int_{\Omega} c^{*}(\cdot, t_n) q(\cdot, t_n) z_h(\cdot, t_n) \, d\mathbf{x}, \qquad \forall z_h(\cdot, t_n) \in S^{c}(\Omega).
\end{aligned} \tag{5.14}$$

To evaluate $z_h(\mathbf{x}, t_{n-1}^{+})$ in Eq. (5.14), we define a characteristic $\mathbf{r}(\theta; \mathbf{x}, t_{n-1})$ by

$$\begin{aligned}
&\frac{d\mathbf{r}}{d\theta} = \frac{\boldsymbol{\sigma}_h^{(m)}(\mathbf{x}, t_n)}{\phi\big(\mathbf{x}, p_h^{(m)}(\mathbf{x}, t_n)\big) \rho\big(p_h^{(m)}(\mathbf{x}, t_n)\big)}, \qquad \theta \in [t_{n-1}, t_n], \\
&\mathbf{r}(\theta; \mathbf{x}, t_{n-1})|_{\theta = t_{n-1}} = \mathbf{x}.
\end{aligned} \tag{5.15}$$

Then we evaluate $z_h(\mathbf{x}, t_{n-1}^{+}) = z_h(\tilde{\mathbf{x}}, t_n)$ with $\tilde{\mathbf{x}} = \mathbf{r}(t_n; \mathbf{x}, t_{n-1})$.

else

We define

$$p_h(\mathbf{x}, t_n) = p_h^{(m)}(\mathbf{x}, t_n), \qquad \boldsymbol{\sigma}_h(\mathbf{x}, t_n) = \boldsymbol{\sigma}_h^{(m)}(\mathbf{x}, t_n), \qquad c_h(\mathbf{x}, t_n) = c_h^{(m)}(\mathbf{x}, t_n). \tag{5.16}$$

endif

end do

6. NUMERICAL EXPERIMENTS

In this section, we present numerical results for several different types of simulations for compressible fluid flows in porous media to observe the performance of the ELLAM-MFEM solution procedure. The numerical experiments simulate compressible fluid flow processes within a horizontal reservoir of one unit thickness over a period of 15 years

TABLE 6.1
Data Used in the Numerical Simulations

Spatial domain	$\Omega = (0, 1000) \times (0, 1000)$ ft^2
Time period of simulation	[0, T] = [0, 5400] days (i.e., 15 years)
Reference porosity	$\phi_r = 0.1$
Compressibility of the medium	$c_\phi = 0.000001.$
Reference density	$\rho_r = 0.8$ g/cm$^3 = 49.942$ lb/ft^3
Compressibility of the fluid	$c_\rho = 0.0001$
Reference pressure	$p_r = 1$ atm. $= 14.696$ psia
Viscosity of the resident fluid (oil)	$\mu_o = 1$ cp
Location of the injection well	(1000, 1000) (i.e., the upper-right corner of Ω)
Location of the production well	(0, 0) (i.e., the lower-left corner of Ω)
Injection rate	$Q = 30$ ft^2/day
Injection concentration	$c_I^* = 1.0$
Production rate	$Q = -30$ ft^2/day
Initial pressure	$p_0(x, y) = 3000$ psia
Initial concentration	$c_0(x, y) = 0.0$
Grid size for pressure	$\Delta x^p = \Delta y^p = 25$ ft
Grid size for concentration	$\Delta x^p = \Delta y^p = 25$ ft
Time step	$\Delta t = 360$ days $= 1$ year

(5400 days), for one-quarter of a regular five-spot pattern with injection and production wells at the corners. The test runs include problems with adverse mobility ratios, tensor dispersion models with various amount of diffusion and dispersion, heterogeneous permeabilities, and heterogeneous media. Few reported data and results can be found in the literature on numerical simulations to the system (2.12)–(2.17), especially with characteristic methods. Hence, whenever it is possible, we try to choose test problems for corresponding incompressible fluid flows (2.20)–(2.21) with reported data and results in the literature. This (i) helps us understand whether the ELLAM-MFEM solution procedure generates physically acceptable solutions and (ii) serves as a way to compare the ELLAM-MFEM solution procedure with many well regarded methods. We understand that this would put the ELLAM-MFEM solution procedure at a disadvantage, because it is used to simulate the compressible fluid flow system (2.12)–(2.17) that has much stronger nonlinearity and couplings than the incompressible fluid flow system (2.20)–(2.21) simulated by other methods. The data used in these experiments are given in Table 6.1.

In Table 6.1, $Q = 30$ ft^2/day is the volumetric flow rate of injection (or production if Q is negative) in the well cells (recall that we have averaged all the physical quantities in the z direction in deriving system (2.12)–(2.17)). The mass flow rate q in Eqs. (2.14) and (2.16) is equal to the product of the mass density ρ and the quantity Q per unit volume [24, 38]. In the numerical experiments, we use a uniform spatial partition $\Delta x^p = \Delta y^p = \Delta x^c = \Delta y^c = 25$ ft (i.e., 40×40 spatial cells) on the domain Ω, although we understand that a nonuniform partition with finer cells around wells could probably generate more accurate solutions and our simulator allows a general partition. We also use an extremely large time step of $\Delta t = 360$ days (1 year). In contrast, in the numerical results reported in the literature previously, the time steps used range from *a few days* for finite difference or finite element simulators to about *a month* for MMOC-based simulators [4, 24, 27, 38, 45, 49, 58] even for the relatively simpler incompressible fluid flow system (2.20)–(2.21).

6.1. Test Problem I: Numerical Simulation in Homogeneous Media

In this section, we carry out numerical simulations to the system (2.12)–(2.17) of compressible fluid flows through homogeneous and isotropic porous media. Besides those in Table 6.1, additional data used in the numerical simulations are presented in Table 6.2.

6.1.1. *Experiments I.1*

In this group of experiments, we perform numerical example runs for porous medium fluid flows, under somewhat idealized assumptions that the mobility ratio between the resident and injected fluids is $M = 1$ and that only molecular diffusion is present in the physical diffusion–dispersion relation (i.e., $D_m = \phi_r d_m = 0.5$ ft^2/day, $D_l = \phi_r d_l = 0.0$ ft, and $D_t = \phi_r d_t = 0.0$ ft). This example has been widely used in the performance testing of a simulator since the qualitative behavior of the physical process is understood fairly well in this case.

The surfaces and contour plots of the simulation at $t = 3$ years (1080 days), at $t = 7$ years (2520 days), at $t = 10$ years (3600 days), and at $t = 15$ years (5400 days) are presented in Fig. 1. It is observed that the solution at $t = 3$ years is a family of concentric circles, as one should expect since the molecular diffusion is homogeneous and the mobility ratio $M = 1$. These results are physically reasonable due to the following reasons: (i) The mobility ratio $M = 1$ implies that the fluid has a constant viscosity $\mu(c) = \mu(0)$. (ii) The facts that $\mathbf{K}$ is a constant tensor and that the reservoir is horizontal lend us to conclude that the mass flow rate $\boldsymbol{\sigma}$ is actually radial. (iii) Only the molecular diffusion, which is isotropic, is assumed to be present. Since in this case the mathematical model does not include any permeability or viscosity variations or mechanical dispersion effects, any fingering phenomenon, if present, would be due to numerical errors and not to the modeling of any physics.

Ideally, if the production well is located at infinity, the solutions should maintain the form of a family of concentric circles that will diffuse gradually. In the current context, because of the effect of the no-flow boundary conditions and the production well, the invading fluid is expected to move toward the production well faster along the diagonal (flow direction). This trend has been observed from the solutions at $t = 7$ years and becomes more obvious in the numerical simulations at $t = 10$ years. By $t = 15$ years, these figures show that the injected fluid has swept all the reservoir and has demonstrated a virtually perfect recovery of the oil in this idealized situation. These results illustrate that even though extremely large time

TABLE 6.2
Additional Data Used in the Experiments I.1 and I.2

Data used in Experiments I.1	
Permeability tensor	$k_{xx} = k_{yy} = 80$ md and $k_{xy} = k_{yx} = 0$ md
Mobility ratio	$M = 1$
Molecular diffusion coefficient	$D_m = \phi_r d_m = 0.5$ ft^2/day
Mechanical dispersion coefficients	$D_l = \phi_r d_l = 0.0$ ft and $D_t = \phi_r d_t = 0.0$ ft
Data used in Experiments I.2	
Permeability tensor	$k_{xx} = k_{yy} = 80$ md and $k_{xy} = k_{yx} = 0$ md
Mobility ratio	$M = 41$
Molecular diffusion coefficient	$D_m = \phi_r d_m = 0.0$ ft^2/day
Mechanical dispersion coefficients	$D_l = \phi_r d_l = 2.0$ ft and $D_t = \phi_r d_t = 0.2$ ft

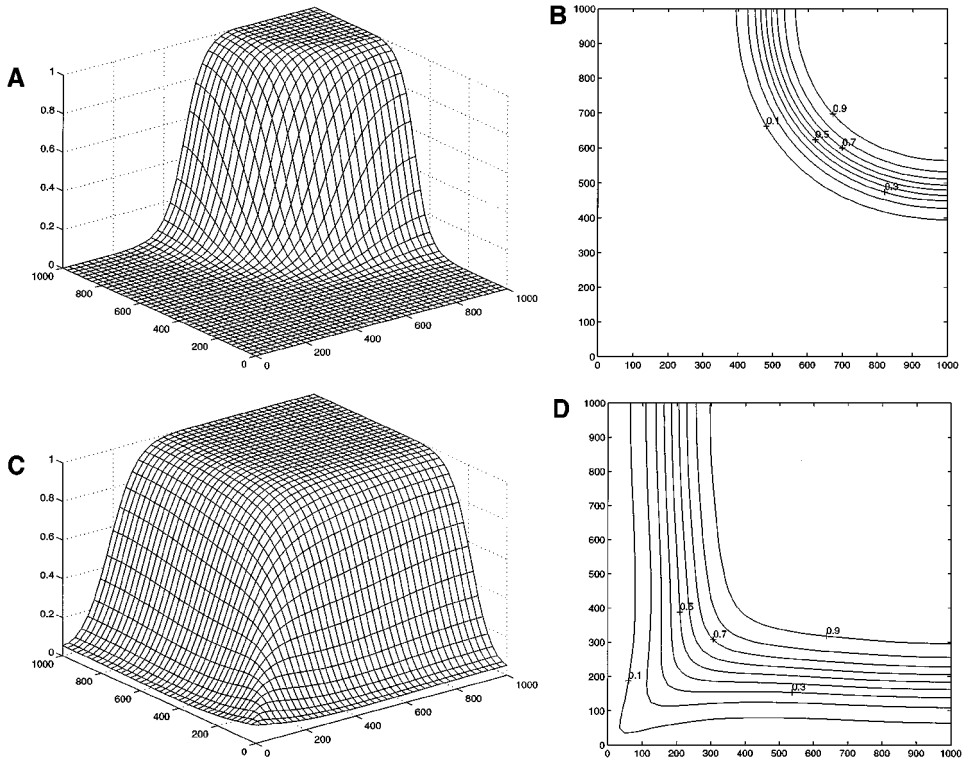

FIG. 1. The concentration plots of the invading component in Experiments I.1 at 3 and 7 years (A–D), and at 10 and 15 years (E–H). (A) Surface plot at $t = 3$ years. (B) Contour plot at $t = 3$ years. (C) Surface plot at $t = 7$ years. (D) Contour plot at $t = 7$ years. (E) Surface plot at $t = 10$ years. (F) Surface plot at $t = 15$ years. (G) Contour plot at $t = 10$ years. (H) Contour plot at $t = 15$ years.

steps and fairly coarse spatial grids have been used in the simulation, the ELLAM-MFEM simulator still generates physically acceptable solutions.

6.1.2. *Experiments I.2*

In this group of experiments, we consider a more realistic simulation in which an adverse mobility ratio of $M = 41$ is used and an anisotropic physical dispersion in tensor form is assumed ($D_m = \phi_r d_m = 0.0\,\text{ft}^2/\text{day}$, $D_l = \phi_r d_l = 2.0\,\text{ft}$, and $D_t = \phi_r d_t = 0.2\,\text{ft}$). The surfaces and contour plots of the simulation at $t = 3$ years, $t = 7$ years, $t = 10$ years, and $t = 15$ years are presented in Fig. 2.

A severe difficulty in the numerical modeling of reservoir simulation is the need to incorporate in the simulation models the bypassing of hydrocarbon due to a viscous fingering phenomenon. Due to the effect of the large adverse mobility ratio $M = 41$, the viscosity $\mu(c)$ changes rapidly across the steep fluid interface. Consequently, the velocity has a rapid change across the fluid interface. Moreover, the large differences in longitudinal versus transverse dispersion levels force the fluid flow to move much faster along the diagonal direction (flow direction) from the injection well to the production well. The plots in Fig. 2 show that the concentration front moves fairly fast in the diagonal direction, which exactly reflects the physical phenomenon of this case. From the point of view of petroleum recovery, this means a much less effective recovery is expected in a realistic petroleum displacement process than in an idealized process in Experiments I.1. We will address this issue more in the next subsection.

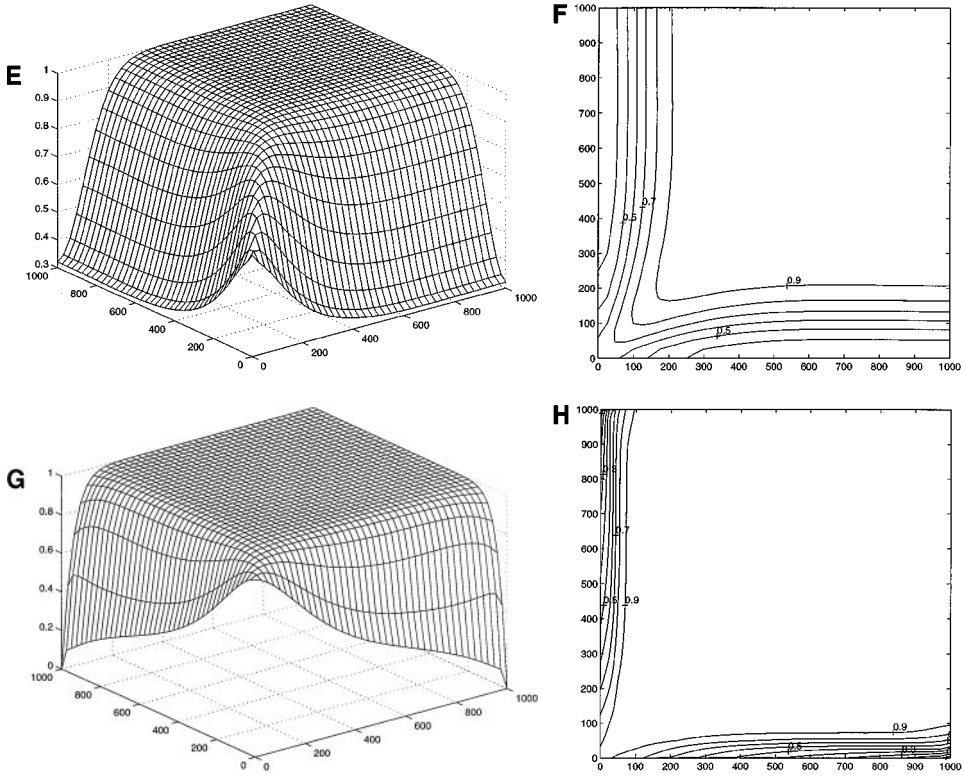

FIG. 1—*Continued*

6.2. Test Problem II: Numerical Simulation in Substructured Media

We consider a numerical simulation to system (2.12)–(2.17) in a substructured medium. The data are given in Table 6.3 in addition to Table 6.1. The surfaces and contour plots of the simulation at $t = 3$ years, $t = 7$ years, $t = 10$ years, and $t = 15$ years are presented in Fig. 3. From these plots, we have the following observations: (i) The ELLAM-MFEM

TABLE 6.3
Additional Data Used in Experiments II

Data in subdomain $\Omega^{(1)}$	
Subdomain	$\Omega^{(1)} = (175, 600) \times (175, 600)$ ft^2
Permeability tensor	$k_{xx} = k_{yy} = 40$ md and $k_{xy} = k_{yx} = 0$ md
Mobility ratio	$M = 41$
Reference porosity	$\phi_r = 0.09$
Molecular diffusion coefficient	$D_m = \phi_r d_m = 0.0$ ft^2/day
Mechanical dispersion coefficients	$D_l = \phi_r d_l = 1.8$ ft and $D_t = \phi_r d_t = 0.18$ ft
Data in subdomain $\Omega^{(2)}$	
Subdomain	$\Omega^{(2)} = \Omega - \Omega^{(1)}$
Permeability tensor	$k_{xx} = k_{yy} = 80$ md and $k_{xy} = k_{yx} = 0$ md
Mobility ratio	$M = 41$
Reference porosity	$\phi_r = 0.1$
Molecular diffusion coefficient	$D_m = \phi_r d_m = 0.0$ ft^2/day
Mechanical dispersion coefficients	$D_l = \phi_r d_l = 2.0$ ft and $D_t = \phi_r d_t = 0.2$ ft

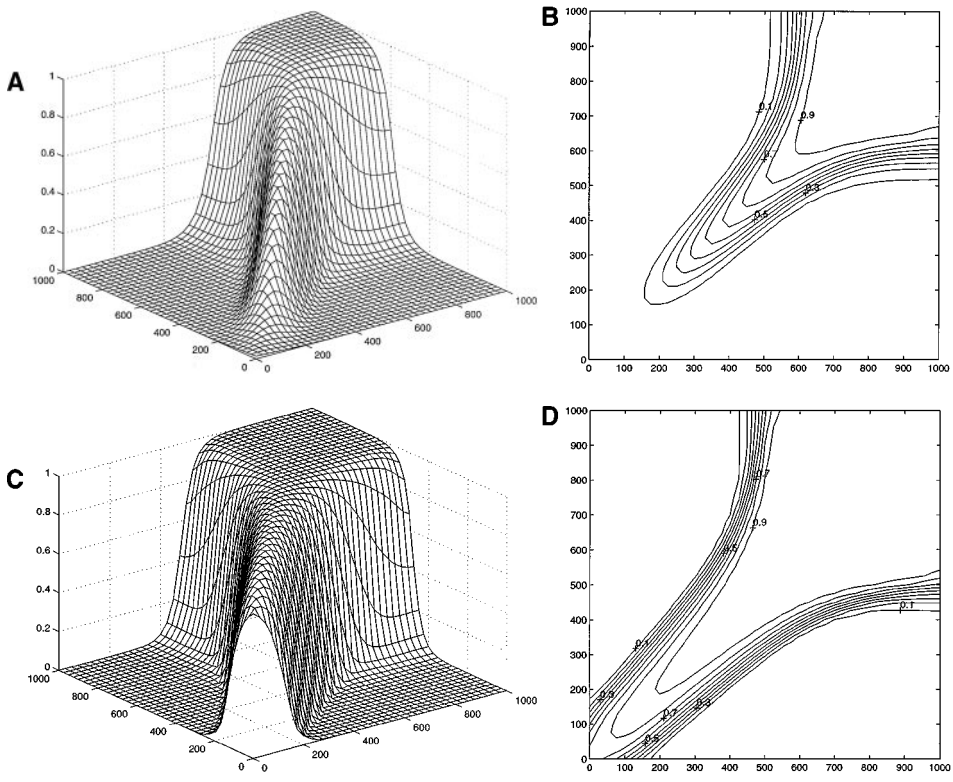

FIG. 2. The concentration plots of the invading component in Experiments I.2 at 3 and 7 years (A–D), and at 10 and 15 years (E–H). (A) Surface plot at $t = 3$ years. (B) Contour plot at $t = 3$ years. (C) Surface plot at $t = 7$ years. (D) Contour plot at $t = 7$ years. (E) Surface plot at $t = 10$ years. (F) Surface plot at $t = 15$ years. (G) Contour plot at $t = 10$ years. (H) Contour plot at $t = 15$ years.

solution procedure developed in this paper generates physically acceptable solutions for a compressible fluid flow through a substructured medium, even though a fairly coarse spatial grid and an extremely large time step are used in the simulation. This in turn implies significantly improved computational efficiency. (ii) The comparison of these results with those in Experiments I.2 shows that whenever possible, one should place the production well in a low-permeability zone to increase the area swept by the injecting fluid (or equivalently the efficiency of the petroleum recovery). This illustrates how the results of numerical simulations could help decision making in the petroleum reservoir industry. (iii) An important technique in enhanced oil recovery is the use of polymers in flooding processes to alter the permeability of the reservoir porous medium to allow flow in certain ways. Since the polymers are highly viscous, they can be used to selectively block or reduce the permeabilities of certain pores or flow regions to direct the flow in a manner to optimize hydrocarbon recovery. The numerical results in this section could also serve as a demonstration for this technique. In this case, the properties of the original fluid and porous medium are given in Table 6.2, while the data in Table 6.3 can be viewed as the altered properties after the injection of some polymers. Then, the solutions in Figs. 2 and 3 illustrate that the displacement process in Experiments II sweeps much larger area, which in turn implies a greatly improved efficiency of the recovery process.

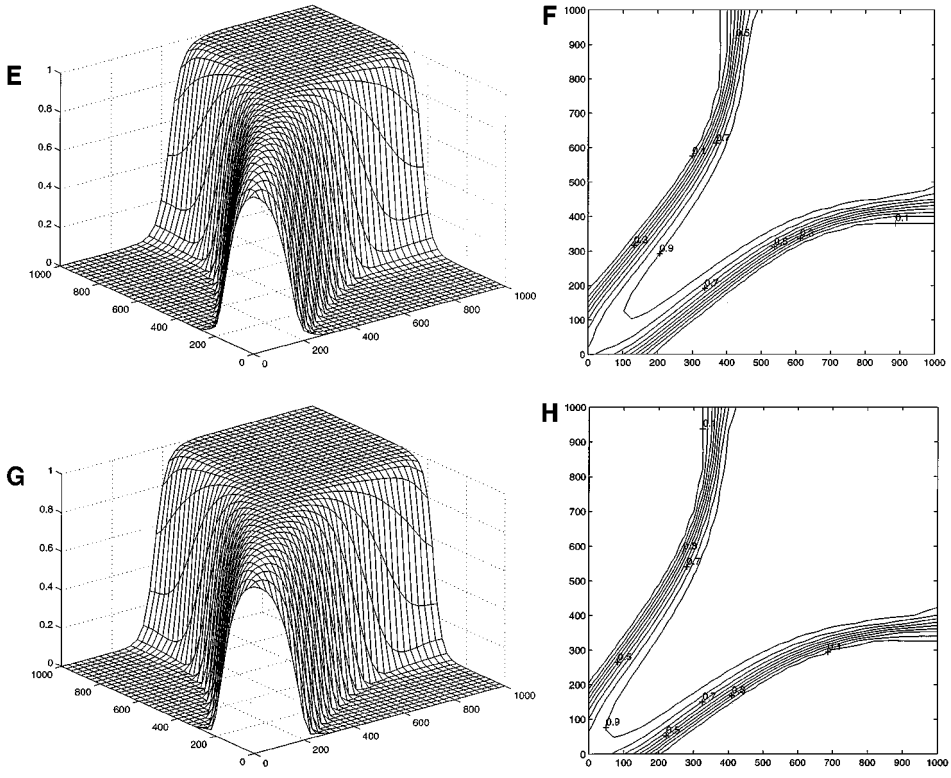

FIG. 2—*Continued*

6.3. Test Problem III: Numerical Simulation in Layered Media

In this section, we carry out numerical simulations to compressible fluid flow processes in layered media, which are often encountered in many field applications.

6.3.1. *Experiments III.1*

We simulate fluid flows in a layered medium in which one highly permeable zone is located between two low permeable zones. The data are given in Table 6.4. The surface and contour plots of the concentration of the invading fluid at $t = 3$ years, $t = 7$ years, $t = 10$ years, and $t = 15$ years are presented in Fig. 4. From Figs. 4A and 4B, we see that the concentration front initially moves faster in the vertical direction than in the horizontal direction, because the subdomain $\Omega^{(2)}$ has a larger permeability and, thus, the mass flow rate σ than that on the subdomain $\Omega^{(1)}$. Once the invading fluid reaches $\Omega^{(2)}$, the concentration front moves much faster in the horizontal direction on $\Omega^{(2)}$ than on $\Omega^{(1)} \cup \Omega^{(3)}$ and exhibits the behavior of a layered flow, due to the same reason. This trend continues as the time evolves, as shown in Figs. 4C–4H.

6.3.2. *Experiments III.2*

We consider the simulation in a layered medium with one low permeable zone between two highly permeable zones, with the data being given in Table 6.5 and the surface and contour plots of the concentration of the invading fluid at $t = 3$ years, $t = 7$ years, $t = 10$ years,

TABLE 6.4
Additional Data Used in Experiments III.1

Data in the first and third layers $\Omega^{(1)} \cup \Omega^{(3)}$	
First layer	$\Omega^{(1)} = (0, 1000) \times (0, 325)$ ft^2
First layer	$\Omega^{(3)} = (0, 1000) \times (675, 1000)$ ft^2
Permeability tensor	$k_{xx} = k_{yy} = 30$ md and $k_{xy} = k_{yx} = 0$ md
Mobility ratio	$M = 41$
Reference porosity	$\phi_r = 0.1$
Molecular diffusion coefficient	$D_m = \phi_r d_m = 0.0$ ft^2/day
Mechanical dispersion coefficients	$D_l = \phi_r d_l = 2.0$ ft and $D_t = \phi_r d_t = 0.2$ ft
Data in the second layer $\Omega^{(2)}$	
Subdomain	$\Omega^{(2)} = (0, 1000) \times (325, 675)$
Permeability tensor	$k_{xx} = k_{yy} = 80$ md and $k_{xy} = k_{yx} = 0$ md
Mobility ratio	$M = 41$
Reference porosity	$\phi_r = 0.1$
Molecular diffusion coefficient	$D_m = \phi_r d_m = 0.0$ ft^2/day
Mechanical dispersion coefficients	$D_l = \phi_r d_l = 2.0$ ft and $D_t = \phi_r d_t = 0.2$ ft

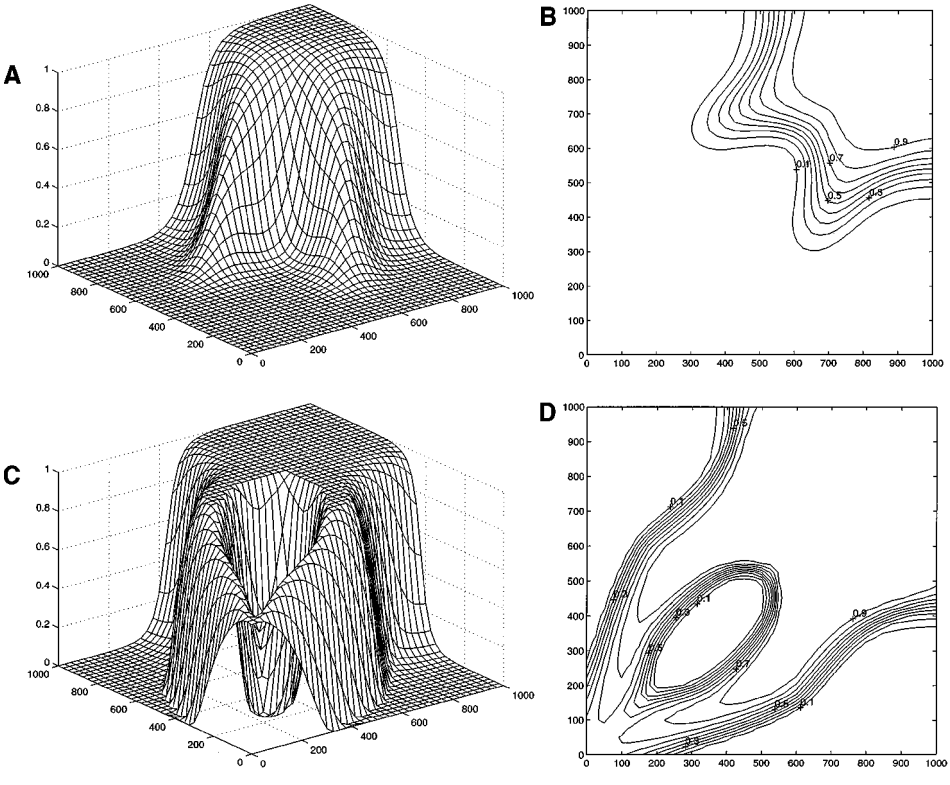

FIG. 3. The concentration plots of the invading component in Experiments II at 3 and 7 years (A–D), and at 10 and 15 years (E–H). (A) Surface plot at $t = 3$ years. (B) Contour plot at $t = 3$ years. (C) Surface plot at $t = 7$ years. (D) Contour plot at $t = 7$ years. (E) Surface plot at $t = 10$ years. (F) Surface plot at $t = 15$ years. (G) Contour plot at $t = 10$ years. (H) Contour plot at $t = 15$ years.

TABLE 6.5
Additional Data Used in Experiments III.2

Data in the first and third layers $\Omega^{(1)} \cup \Omega^{(3)}$	
First layer	$\Omega^{(1)} = (0, 1000) \times (0, 325)$ ft^2
First layer	$\Omega^{(3)} = (0, 1000) \times (675, 1000)$ ft^2
Permeability tensor	$k_{xx} = k_{yy} = 80$ md and $k_{xy} = k_{yx} = 0$ md
Mobility ratio	$M = 41$
Reference porosity	$\phi_r = 0.1$
Molecular diffusion coefficient	$D_m = \phi_r d_m = 0.0$ ft^2/day
Mechanical dispersion coefficients	$D_l = \phi_r d_l = 2.0$ ft and $D_t = \phi_r d_t = 0.2$ ft
Data in the second layer $\Omega^{(2)}$	
Subdomain	$\Omega^{(2)} = (0, 1000) \times (325, 675)$
Permeability tensor	$k_{xx} = k_{yy} = 30$ md and $k_{xy} = k_{yx} = 0$ md
Mobility ratio	$M = 41$
Reference porosity	$\phi_r = 0.1$
Molecular diffusion coefficient	$D_m = \phi_r d_m = 0.0$ ft^2/day
Mechanical dispersion coefficients	$D_l = \phi_r d_l = 2.0$ ft and $D_t = \phi_r d_t = 0.2$ ft

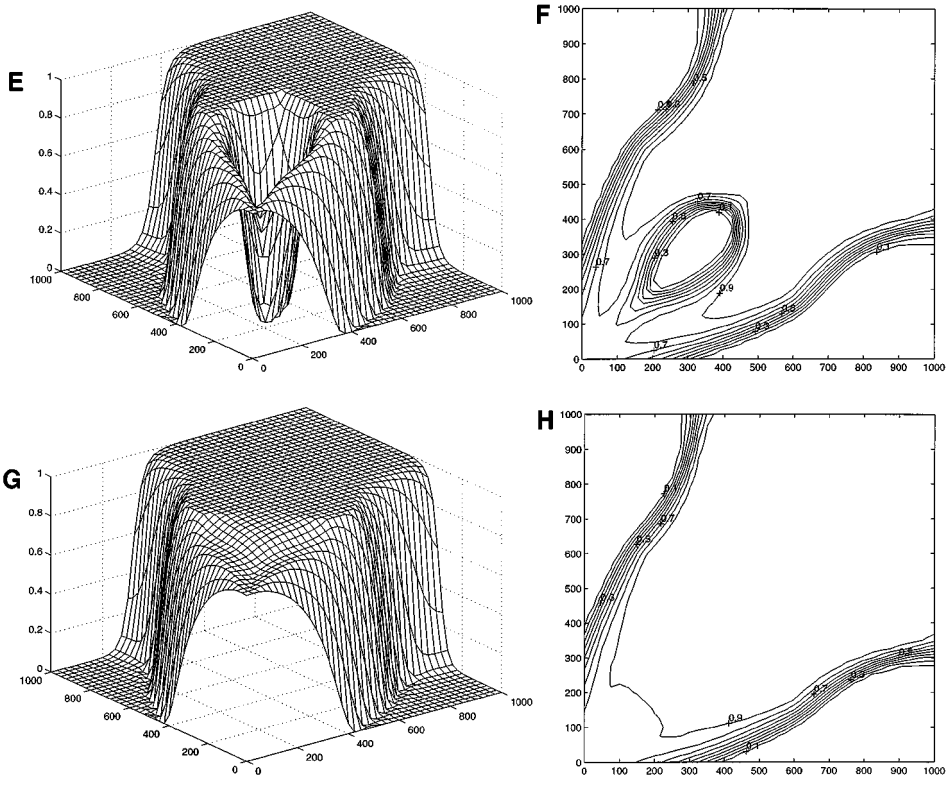

FIG. 3—*Continued*

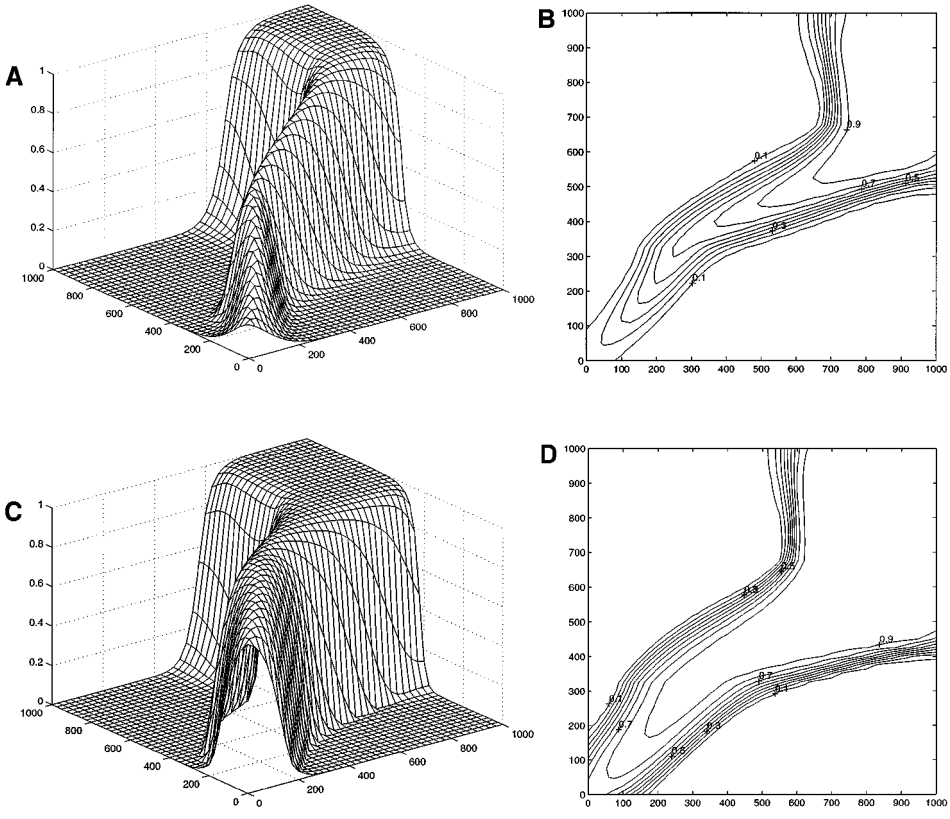

FIG. 4. The concentration plots of the invading component in Experiments III.1 at 3 and 7 years (A–D), and at 10 and 15 years (E–H). (A) Surface plot at $t = 3$ years. (B) Contour plot at $t = 3$ years. (C) Surface plot at $t = 7$ years. (D) Contour plot at $t = 7$ years. (E) Surface plot at $t = 10$ years. (F) Surface plot at $t = 15$ years. (G) Contour plot at $t = 10$ years. (H) Contour plot at $t = 15$ years.

and $t = 15$ years being presented in Fig. 5. They show that the concentration front slows down once it moves into the subdomain $\Omega^{(2)}$, because $\Omega^{(2)}$ has a smaller permeability and, thus, smaller mass flow rate $\boldsymbol{\sigma}$ is larger than that on the subdomain $\Omega^{(1)}$. The plots at $t = 7$ years and $t = 10$ years demonstrate that the concentration front at the right half of Ω is rapidly catching up with the main flow path in the diagonal direction and forms some fingering. The corresponding displacement process of the invading fluid becomes much more complex and the fingering phenomena occurs.

In summary, the numerical simulation of fluid flow processes in multi-layered porous media could encounter serious fingering problems. Note that the governing equations (2.14) and (2.16) in the systems of compressible fluid flows (2.12)–(2.17) are obtained via a volume averaging mechanism that does not model physical behavior on a pore-volume scale. Because the mathematical model now includes differences in longitudinal versus transverse dispersion levels, these equations should model the corresponding behavior of the flow in the form of a macroscopic fingering phenomenon due to varying flow velocities, which should propagate and grow in a manner similar to viscous fingering on a smaller scale.

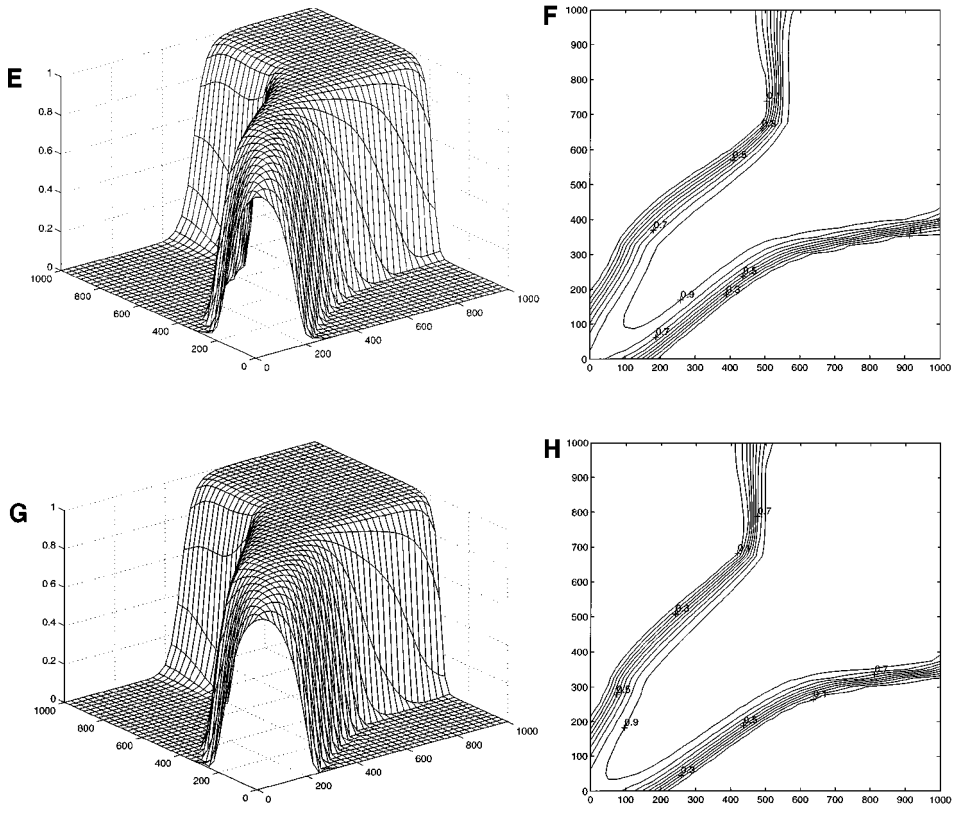

FIG. 4—*Continued*

7. SUMMARY AND CONCLUSIONS

In this paper we develop an ELLAM-MFEM sequential decoupling and linearization solution procedure for compressible fluid flows in porous media with point sources and sinks (injection and production wells), in which we use an Eulerian–Lagrangian localized adjoint method to solve the transport equation (2.16) for the concentration c and a mixed finite element method to solve the pressure equation (2.14) for the pressure p and the mass flow rate $\boldsymbol{\sigma}$. The ELLAM-MFEM solution procedure symmetrizes the governing transport equation, and greatly reduces or eliminates non-physical oscillation and/or excessive numerical dispersion present in many large-scale simulators that are widely used in industrial applications. In addition, the ELLAM-MFEM solution procedure conserves mass and treats boundary conditions in a natural manner. The numerical experiments also illustrate that the ELLAM-MFEM solution procedure can simulate compressible fluid flows in porous media accurately with fairly coarse spatial grids as well as very large time steps, which are much larger than the time steps used in the MMOC-MFEM sequential solution procedure and one or two orders of magnitude larger than those used in many large-scale simulators. In this manner, the ELLAM-MFEM solution technique has a greatly improved computational efficiency over many other methods. Finally, the ELLAM-MFEM technique can treat large adverse mobility ratios, discontinuous permeabilities and porosities, anisotropic dispersion

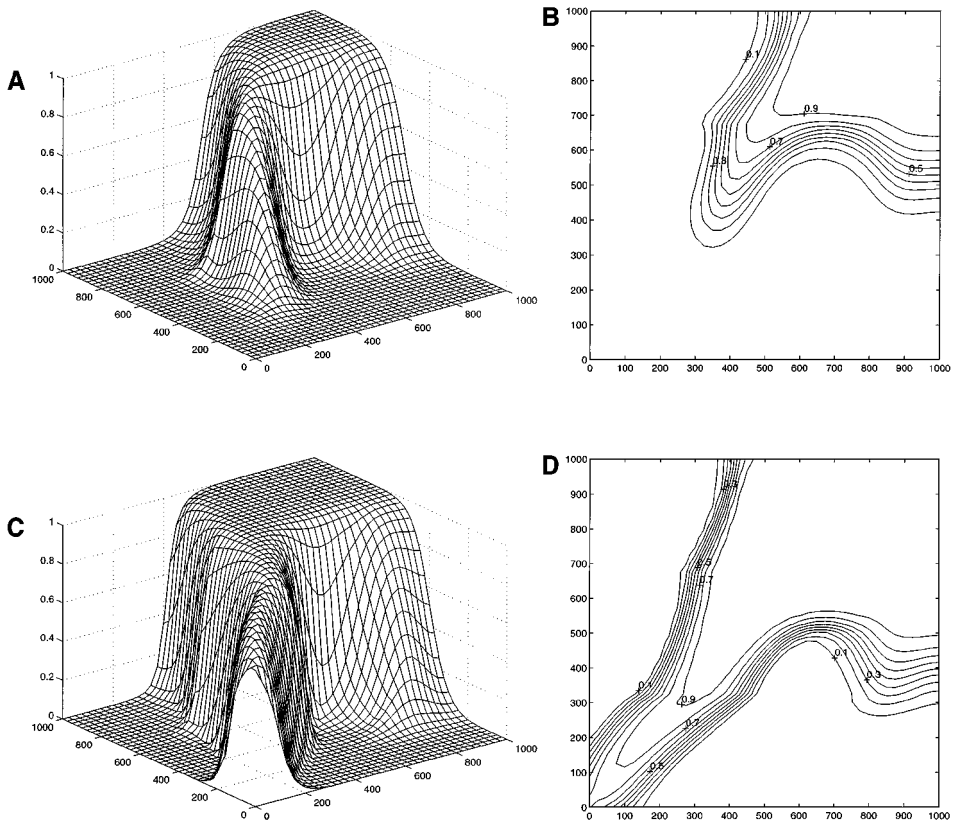

FIG. 5. The concentration plots of the invading component in Experiments III.2 at 3 and 7 years (A–D), and at 10 and 15 years (E–H). (A) Surface plot at $t = 3$ years. (B) Contour plot at $t = 3$ years. (C) Surface plot at $t = 7$ years. (D) Contour plot at $t = 7$ years. (E) Surface plot at $t = 10$ years. (F) Surface plot at $t = 15$ years. (G) Contour plot at $t = 10$ years. (H) Contour plot at $t = 15$ years.

in tensor form, compressible fluid and media, heterogeneous media, and point sources and sinks.

Because system (2.14)–(2.16) and its variety of modifications hold in many applications, the ELLAM-MFEM solution technique (possibly with slight modifications) developed in this paper could be applied to many other fields in addition to petroleum reservoir simulation. For example, the ELLAM-MFEM technique can be used in the simulation of subsurface environmental modeling and/or remediation in fully saturated zone, since the mathematical model (2.14)–(2.16) still holds in this case. For a subsurface flow process through an unsaturated zone above the water table, the pressure PDE (2.14) could be replaced by the Richards equation [44], while the tranport PDE (2.16) still holds. The Richards equation can be solved by an appropriately modified version of the MFEM scheme in Section 3 (see [9] and the references therein), while the transport equation (2.16) can be solved again by the ELLAM scheme in Section 4. In principle, we can apply the ELLAM method to solve the systems in which the transport PDEs are linear in their primary unknown variables. We refer readers to the work of Ewing [25] if the transport PDEs are nonlinear in the primary unknowns.

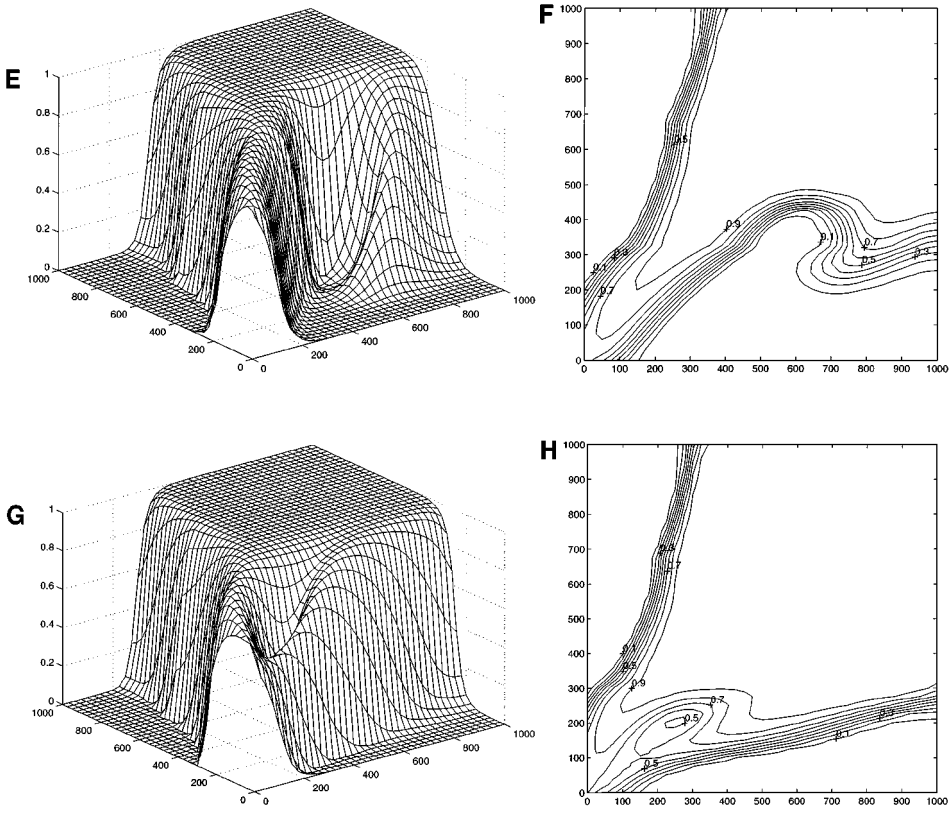

FIG. 5—*Continued*

REFERENCES

1. M. Al-Lawatia, R. C. Sharpley, and H. Wang, Second-order characteristic methods for advection–diffusion equations and comparison to other schemes, *Adv. Water Resources* **22**, 741 (1999).
2. T. Arbogast and Z. Chen, On the implementation of mixed methods as nonconforming methods for second-order elliptic problems, *Math. Comp.* **64**, 943 (1995).
3. D. N., Arnold and F. Brezzi, Mixed and nonconforming finite element methods: Implementations, postprocessing, and error estimates, *RARIO Modél. Math. Anal. Numér.* **19**, 7 (1985).
4. H. Aziz and A. Settari, *Petroleum Reservoir Simulation* (Applied Science, 1979).
5. I. Babuška, J. T. Oden, and J. L. Lee, Mixed-hybrid finite element method approximations of second-order elliptic boundary value problems, Part 1, *Comput. Methods Appl. Mech. Engrg.* **11**, 175 (1977).
6. P. L. Bansal, J. L. Harper, A. E. McDonald, E. E. Moreland, A. S. Odeh, and R. H. Trimble, *A Strongly Coupled Fully Implicit, Three-Dimensional, Three-Phase Reservoir Simulator*, SPE 8329, 1979.
7. J. Bear, *Hydraulics of Groundwater* (McGraw–Hill, New York, 1979).
8. J. P. Benque and J. Ronat, Quelques difficulties des modeles numeriques en hydraulique, in *Computing Methods in Applied Sciences and Engineering*, edited by Glowinski and Lions (North-Holland, Amsterdam, 1982), p. 471.
9. P. J. Binning, *Modeling Unsaturated Zone Flow and Contaminant in the Air and Water Phases*, Ph.D. thesis, Department of Civil Engineering and Operational Research, Princeton University, 1994.
10. J. H. Bramble and E. Pasciak, A preconditioning technique for indefinite systems resulting from mixed approximations of elliptic problems, *Math. Comp.* **50**, 1 (1988).
11. F. Brezzi, On the existence, uniqueness and approximation of saddle-point problems arising from Lagrangian multipliers, *RARIO Modél. Math. Anal. Numér.* **8**, 129 (1974).

12. F. Brezzi and M. Fortin, *Mixed and Hybrid Finite Element Methods*, Springer Series in Computational Mathematics, Vol. 15 (Springer-Verlag, New York, 1991).
13. M. A. Celia, T. F. Russell, I. Herrera, and R. E. Ewing, An Eulerian–Lagrangian localized adjoint method for the advection–diffusion equation, *Adv. Water Resources* **13**, 187 (1990).
14. H. Chen. R. E. Ewing, S. L. Lyons, G. Qin, T. Sun, and D. P. Yale, Numerical solution of coupled geomechanics and fluid flow in elastic porous media, in *Proceedings of International Workshop on Computational Physics: Fluid Flow and Transport in Porous Media, State of the Art, Beijing, China, 1999*, edited by Z. Chen, R. E. Ewing, and Z. Shi, Lecture Notes in Physics (Springer-Verlag, New York, in press).
15. C. Chu, K. H. Coats, W. D. George, and B. E. Marcum, Three-dimensional simulation of steam flooding. *SPE J. Trans. AIME* **14**, 573 (1974).
16. P. Colella, A direct Eulerian MUSCL scheme for gas dynamics, *SIAM J. Sci. Comput.* **6**, 104, (1985).
17. R. Courant, E. Isaacson, and M. Rees, On the solution of nonlinear hyperbolic differential equations by finite differences, *Comm. Pure. Appl. Math.* **5**, 243 (1952).
18. M. G. Crandall and A. Majda, Monotone difference approximations for scalar conservation laws, *Math. Comp.* **34**, 1 (1980).
19. B. L. Darlow, R. E. Ewing, and M. F. Wheeler, Mixed finite element methods for miscible displacement problems in porous media, SPE 10501, *Soc. Pet. Eng. J.* **24** (1984), 391–398.
20. J. Douglas, Jr., R. E. Ewing, and M. F. Wheeler, The approximation of the pressure by a mixed method in the simulation of miscible displacement, *RARIO Modél. Math. Anal. Numér.* **17**, 17 (1983).
21. J. Douglas, Jr., R. E. Ewing, and M. F. Wheeler, A time-discretization procedure for a mixed finite element approximation of miscible displacement in porous media, *RARIO Modél. Math. Anal. Numér.* **17**, 249 (1983).
22. J. Douglas, Jr., and T. F. Russell, Numerical methods for convection-dominated diffusion problems based on combining the method of characteristics with finite element or finite difference procedures, *SIAM J. Numer. Anal.* **19**, 871 (1982).
23. B. Einfeldt, On Godunov-type methods for gas dynamics, *SIAM J. Numer. Anal.* **25**, 294 (1988).
24. R. E. Ewing (Ed.), *The Mathematics of Reservoir Simulation*, Research Frontiers in Applied Mathematics, Vol. 1 (SIAM, Philadelphia, 1984).
25. R. E. Ewing, Operator splitting and Eulerian–Lagrangian localized adjoint methods for multiphase flow, in *The Mathematics of Finite Elements and Applications VII* (MAFELAP, 1990), edited by J. R. Whiteman (Academic Press, San Diego, CA, 1991), p. 215.
26. R. E. Ewing and R. F. Heinemann, Mixed finite element approximation of phase velocities in compositional reservoir simulation, *Comput. Methods Appl. Mech. Engrg.* **47**, 161 (1984).
27. R. E. Ewing, T. F. Russell, and M. F. Wheeler, *Simulation of Miscible Displacement Using Mixed Methods and a Modified Method of Characteristics*, SPE 12241, 1983, p. 71.
28. R. E. Ewing, H. Wang, M. A. Celia, and R. C. Sharpley, A three-dimensional finite element simulation of nuclear waste contamination transport in porous media, in *Computer Methods and Advances in Geomechanics*, Vol. 9, edited by Siriwardane and Zaman (Balkema, Rotterdam, Netherlands/Brookfield, 1995), p. 2673.
29. A. O. Garder, D. W. Peaceman, and A. L. Pozzi, Numerical calculations of multidimensional miscible displacement by the method of characteristics, *Soc. Pet. Eng. J.* **4**, 26 (1964).
30. V. Girault and P. A. Raviart, Finite element methods for Navier–Stokes equations: Theory and algorithms, in Lecture Notes in Computational Mathematics, Vol. 5 (Springer-Verlag, Berlin, 1986).
31. A. Harten, B. Engquist, S. Osher, and S. Chakravarthy, Uniformly high order accurate essentially nonoscillatory schemes, III, *J. Comput. Phys.* **71**, 231 (1987).
32. R. W. Healy and T. F. Russell, A finite-volume Eulerian–Lagrangian localized adjoint method for solution of the advection–dispersion equation, *Water Resources Res.* **29**, 2399 (1993).
33. I. Herrera, R. E. Ewing, M. A. Celia, and T. F. Russell, Eulerian–Lagrangian localized adjoint methods: The theoretical framework, *Numer. Methods Partial Differential Equations* **9**, 431 (1993).
34. D. Hillel, *Fundamentals of Soil Physics* (Academic Press, New York, 1980).
35. R. W. Lewis and B. A. Schrefler, *The Finite Element Methods in the Static and Dynamic Deformation and Consolication of Porous Media* (Wiley, New York, 1998).

36. L. D. Marini, An inexpensive method for the evaluation of the solution of the lowest order Raviart–Thomas mixed method, *SIAM J. Numer. Anal.* **22**, 493 (1985).
37. S. P. Neuman, An Eulerian–Lagrangian numerical scheme for the dispersion–convection equation using conjugate space-time grids, *J. Comput. Phys.* **41**, 270 (1981).
38. D. W. Peaceman, *Fundamentals of Numerical Reservoir Simulation* (Elsevier, Amsterdam, 1977).
39. O. Pironneau, On the transport-diffusion algorithm and its application to the Navier–Stokes equations, *Numer. Math.* **38**, 309 (1982).
40. D. W. Pollock, Semianalytical computation of path lines for finite-difference models, *Ground Water* **26**, 743 (1988).
41. J. Pudykiewicz and A. Staniforth, Some properties and comparative performance of the semi-Lagrangian method of Robert in the solution of the advection–diffusion equation, *Atmosphere Ocean* **22**, 283 (1984).
42. P. A. Raviart and J. M. Thomas, A mixed finite element method for second order elliptic problems, in *Mathematical Aspects of Finite Element Methods*, edited by I. Gulligani and E. Magenes, Lecture Notes in Mathematics, Vol. 606 (Springer-Verlag, Berlin, 1977), p. 292.
43. R. C. Reid, J. M. Prausnitz, and B. E. Poling, *The Properties of Gases & Liquids*, 4th ed. (McGraw–Hill, New York, 1987).
44. L. A. Richards, Capillary conduction of liquids through porous media, *Physics* **1**, 318 (1931).
45. T. F. Russell, Finite elements with characteristics for two-component incompressible miscible displacement, SPE 10500, in *Proc. 6th SPE Symposium on Reservoir Simulation, New Orleans, 1982*, p. 123.
46. T. F. Russell and R. V. Trujillo, Eulerian–Lagrangian localized adjoint methods with variable coefficients in multiple dimensions, in *Computational Methods in Surface Hydrology, Proceedings of the Eighth International Conference on Computational Methods in Water Resources, Venice, Italy, 1990*, p. 357.
47. T. F. Russell and M. F. Wheeler, Finite element and finite difference methods for continuous flows in porous media, in *The Mathematics of Reservoir Simulation*, edited by R. E. Ewing (SIAM, Philadelphia, 1984), p. 35.
48. A. L. Schafer-Perini and J. L. Wilson, Efficient and accurate front tracking for two-dimensional groundwater flow models, *Water Resources Res.* **27**, 1471 (1991).
49. A. Settari, H. S. Price, and T. Dupont, Development and application of variational methods for simulation of miscible displacement in porous media, *Soc. Pet. Eng. J.*, 228 (1977).
50. C. Shu and S. Osher, Efficient implementation of essentially non-oscillatory shock capturing schemes, *J. Comput. Phys.* **77**, 439 (1988).
51. P. K. Sweby, High resolution schemes using flux limiters for hyperbolic conservation laws, *SIAM J. Numer. Anal.* **21**, 995 (1984).
52. D. P. Tassios, *Applied Chemical Engineering Thermodynamics* (Springer-Verlag, New York, 1993).
53. B. van Leer, On the relation between the upwind-differencing schemes of Godunov, Engquist-Osher, and Roe, *SIAM J. Sci. Comput.* **5**, 1 (1984).
54. E. Varoglu and W. D. L. Finn, Finite elements incorporating characteristics for one-dimensional diffusion–convection equation, *J. Comput. Phys.* **34**, 371 (1980).
55. H. Wang, M. Al-Lawatia, and S. A. Telyakovskiy, A Runge–Kutta characteristic method for first-order linear hyperbolic equations, *Numer. Methods Partial Differential Equations* **13**, 617 (1997).
56. H. Wang, R. E. Ewing, G. Qin, S. L. Lyons, M. Al-Lawatia, and S. Man, A family of Eulerian–Lagrangian localized adjoint methods for multi-dimensional advection-reaction equations, *J. Comput. Phys.* **152**, 120 (1999).
57. H. Wang, R. C. Sharpley, and S. Man, An ELLAM scheme for advection–diffusion equations in multi-dimensions, in *Computational Methods in Water Resources XI*, Vol. 2, edited by Aldama *et al*. (Computational Mechanics, Southampton/Boston, 1996), p. 99.
58. L. C. Young, A finite element method for reservoir simulation, *Soc. Pet. Eng. J.*, 115 (1981).